Fall 2018

BROADBAND ACOUSTIC MEASUREMENTS OF A CONTROLLED SEEP WITH MULTIPLE GASES FOR VERIFICATION OF FLUX ESTIMATES THROUGH BUBBLE DISSOLUTION AND TARGET STRENGTH MODELS

Kevin Michael Rychert
University of New Hampshire, Durham

BROADBAND ACOUSTIC MEASUREMENTS OF A CONTROLLED SEEP WITH MULTIPLE GASES FOR VERIFICATION OF FLUX ESTIMATES THROUGH BUBBLE DISSOLUTION AND TARGET STRENGTH MODELS

BY

KEVIN RYCHERT

B.S. Physics, University of New Hampshire, 2011

THESIS

Submitted to the University of New Hampshire

in Partial Fulfillment of

The Requirements for the Degree of

Master of Science

in

Ocean Engineering: Ocean Mapping

September, 2018

This thesis has been examined and approved in partial fulfillment of the requirements for the degree of Master of Science in Ocean Engineering: Ocean Mapping by:

Thesis Director, Thomas Weber, Associate Professor, Mechanical Engineering

Larry Mayer, Professor, Earth Sciences

Anthony Lyons, Research Professor, Center for Coastal and Ocean Mapping

On May 4th 2018

Original approval signatures are on file with the University of New Hampshire Graduate School

ACKNOWLEDGEMENTS

I would like to thank Dr. Thomas Weber for guidance as my thesis advisor, for providing me the opportunity to work on this research in pursuit of my interest in ocean engineering. I would like to thank my thesis committee and all the faculty, students and staff at CCOM who have helped conduct and influence this graduate research here over the past two years. This work was funded by NSF grant #1352301 and Exxon-Mobil URC.

Table of Contents

Abstract

BROADBAND ACOUSTIC MEASUREMENTS OF A CONTROLLED SEEP WITH MULTIPLE GASES FOR VERIFICATION OF FLUX ESTIMATES THROUGH BUBBLE DISSOLUTION AND TARGET STRENGTH MODELS

by

Kevin Rychert

University of New Hampshire, September 2018

To verify existing models for conversion of acoustic target strength to estimates of the total volume of methane gas released from the seafloor through the water column, a synthetic seep system was designed and fabricated. This system creates individual bubbles of the sizes most commonly found in gaseous methane seeps, <1 to 5mm radii, which can be released at any interval at depths up to 200m. The synthetic seep system was deployed off the coast of New Hampshire adjacent to the Isles of Shoals to a depth of 55m. Acoustic backscatter from 16-24kHz was collected by steaming over the synthetic seep multiple times with a suite of broadband splitbeam sonar systems. Each iteration ensonified a predetermined and calibrated bubble size created by the system at depth. These data represent a direct field measurement which was used to test models describing bubble evolution and acoustic scattering during the ascent through the water column for bubbles of different sizes and gasses. Validating these models directly tests the ability of broadband sonar systems to estimate the transport of gas from the seabed to the ocean and atmosphere. Acoustic data from 2.35mm radii argon bubbles, and 2.45mm radii nitrogen bubbles are consistent with bubble evolution and target strength models which validates spherical approximations made in both the mass transfer and acoustic scattering assumptions. Based on the similar uncertainty values for these bubble sizes, these data add confidence to the claims of previous studies which use similar methods for methane flux approximations.

I. Introduction

i. Methane Seeps and Bubble Fate

Methane escapes from the seabed though gaseous seeps, and plays an important role as a greenhouse in global climate change. The amount of methane released from hydrate deposits into the ocean and atmosphere, has been linked with the increase in ocean temperature over a short time interval during the latest Paleoscene period ~56 million years ago [Dickens et al. 1995]. Currently, increasing temperatures cause additional methane release which in turn increases the temperature through greenhouse effect, continuing this cycle. Methane seeps have been observed in the water column emanating from the seabed in many environments throughout the world. The location of a seep plays an important role in the fate of the gas it releases, whether it is absorbed into the water column or survives to the surface releasing methane directly into the atmosphere. Seeps can form from biogenic or thermogenic sources, commonly emanating from hydrates on the seabed [Judd et al. 2004]. Hydrate formation in these sources depends on the temperature and hydrostatic pressure of the methane [Collett et al. 2009].

Although the exact fate of the methane from these seeps is uncertain, it can be better understood by examining the individual components which impact the bubbles as they traverse through the water column. As a bubble rises, it expands in size and volume due to the decreasing hydrostatic pressure, while simultaneously exchanging gas with the surrounding water. The rate at which this exchange occurs has been modeled by McGinnis et al. (2006), for a variety of gasses including, methane, argon, and nitrogen. In the deep ocean, typically at depths greater than 1000m, this becomes more complicated through hydrate formation on the outside of the bubble. The gas

transfer is effected by this hydrate coating in addition to the accumulation of particulate or oil on the surface of the bubble, which can occur at the orifice of formation on the seabed or during the vertical transport, resulting in complicated gas transfer through the interface between the internal gas and surrounding water [Rehder et al. 2002]. The bubbles from deeper seeps rarely make it to the surface, dissolving completely during ascent due to the low aqueous concentration of methane in the surrounding water. The methane content from bubbles which survives to the surface is greatly diluted from the original concentration during this travel [McGinnis et al. 2006]. Thus, much of the atmospheric methane released directly to the atmosphere derives from shallow methane seeps closer to the surface on the continental shelf.

The quantification of methane gas released into the ocean and atmosphere from these seeps has been attempted by a variety of methods. Some examples include using an ROV and an inverted cylinder for camera based volumetric measurements [Weber et al. 2014], direct optical measurements of bubbles in the plume [Leifer et al. 2003, Wang et al. 2010], and using remote broadband acoustic echosounders [Weber et al. 2014]. Optical measurements are expensive and time consuming relative to remote sensing, and are unsuited for large scale studies of methane release. The remote acoustic observations of gaseous methane seeps from the seafloor are used to approximate the flow rate based on the frequency response and relative backscatter target strength of the signal [Weber et al. 2014].

To test the validity of the assumptions made in the evolution and acoustic scattering models, a synthetic seep generator was designed and fabricated to precisely control the flow rate, size, and gas composition of the bubbles. The system creates individual bubbles calibrated to sizes in the most common range of 1-5mm, released at any frequency, directly controlling the flow rate. The

synthetic seep was deployed off the coast of New Hampshire adjacent to the Isles of Shoals to a depth of 55m and acoustic backscatter from 16-24kHz was collected by steaming over the synthetic seep multiple times with a suite of broadband splitbeam sonar systems. Each iteration ensonified a predetermined and calibrated bubble size created by the system at depth. These data represent a ground truth measurement, which directly test the ability of broadband sonar systems to estimate the transport of methane gas from seabed to the ocean and atmosphere through bubble evolution and target strength models. The details of the models, and the experiment carried out are described in the following sections.

II. Bubble Models

Mathematical models for bubble evolution and acoustic scattering strength are used together to predict methane flux from gas seeps. The assumptions these models make, however, could limit their validity if the underlying assertions made are not true. There are potential shortcomings with both models. The gas dissolution rate assumes the surface is clean and uncoated by surfactants, oils, or hydrates, this has implications for the gas transfer. Both models assume the bubble is spherical, which affects the surface area of the bubble and the physics of how the water-gas system rings when excited. Laboratory observations of stable bubbles over long periods suggest that the dissolution rate may be slower, and a more complicated phenomenon is occurring [Johnson and Cooke 1981]. While it may have been difficult to rigorously test each of these assumptions through individual experimentation, these models were examined directly by controlling variables, bubble size and gas composition, specifically, limiting the number of unknowns. This research seeks to

answer the question of whether these assumptions are reasonable through direct ground truth measurements.

i. Fate, Evolution, and Dissolution

The dynamics of the fate of a bubble released from the seabed has been discussed and modeled by McGinnis et al. (2006). This model considers several factors which affect the bubble as it rises through the water column. The balance between the hydrostatic pressure decrease and the internal pressure of the bubble causes the compressed gas volume to expand. At the same time, the gases within the bubble and the aqueous gas concentrations in the surrounding water cause mass transfer in both directions through the gas-water interface. For example, if a bubble begins with 100% CH_4 concentration, and the aqueous concentration of the surrounding water is 0%, the methane will transfer to the water, and the dissolved gasses in the water, e.g. O_2, N_2, CO_2, will transfer into the bubble. The rate of the transfer between the gas and liquid depends on the relative concentrations of gasses in each substance. The other factors which effect this rate are: 1) the size of the bubble; 2) interface surface area; 3) bubble rise velocity; 4) Henry's law coefficient; 5) diffusion coefficient; 6) temperature and salinity of the surrounding water, and; 7) the gas transfer velocity, K [Liss 1973, Leifer and Patro 2002]. The parameter, K, has a complex dependency based on the cleanliness of the bubble surface, the depth and the size of the bubble, and the relative gas concentrations interior and exterior to the bubble.

For this experiment, since the artificial seep created clean bubbles, K was set based on the clean bubble curve, and generally to a value which is assumed to be unaffected by any coating or dirt.

The assumption is that the bubble does not collect a significant amount of oil or other surfactant while rising though the water column at the deployment sites off the coast of New Hampshire. Leifer and Patro (2002) derive the equation of state for the change in bubble radius by using a modified gas law, equation 1:

$$P_bV=ZNRT \quad [1]$$

Where P_b is the internal pressure of the bubble, V is the volume, Z is the compressibility factor from the Peng-Robinson equation of state [Obrey 1998], N is the number of moles, R is the universal gas constant, and T is the temperature. With respect to time in equation 2:

$$P_b\frac{dV}{dt}V\frac{dP}{dt} = ZRT\frac{dN}{dt} \quad [2]$$

Since the pressure of the bubble is $P_{atm +} \rho gh + 2\frac{\tau}{r}$, where ρ is the density of the water, g is the gravitational constant, h is the depth of the bubble, and τ is the surface tension of the bubble, it is possible to combine this with equation 2 and substitute the volume of a sphere in order to obtain equation 3:

$$P_b\ (4\pi r^2\frac{dr}{dt})+ \frac{4}{3}\pi r^3\ ((\rho g\frac{dh}{dt})- \frac{dr}{dt}\ (2\ \frac{\tau}{r^2})) = ZRT\frac{dN}{dt} \quad [3]$$

Rearranging equation 3 to solve for the effective radius of the bubble, it is possible to show that the radius over time can be given by equation 4 [Leifer, 2002]:

$$\frac{dr}{dt} = \frac{RT\left(Z_{CH_4}\frac{dNCH_4}{dt}+Z_{O_2}\frac{dNO_2}{dt}+Z_{N_2}\frac{dNN_2}{dt}\right)-\frac{4\pi r^3}{3}\rho_{H_2O}g\frac{dz}{dt}}{4\pi r^2 P_b-\frac{8\pi r\tau}{3}} \quad [4]$$

There are three terms contained in equation 4 which combine in the dissolution model, the first, $RT\left(Z_{CH_4}\frac{dNCH_4}{dt}+Z_{O_2}\frac{dNO_2}{dt}+Z_{N_2}\frac{dNN_2}{dt}\right)$, describes the amount of gas in the bubble, the second, $(\frac{4\pi r^3}{3}\rho_{H_2O}g\frac{dz}{dt})$, is the change in volume due to change in hydrostatic pressure, and the third, $4\pi r^2 P_b-\frac{8\pi r\tau}{3}$, is the pressure inside the bubble based on the bubbles radius and surface tension. Where equation 5 from [Liss 1973, Leifer and Patro 2002] resolves the mass transfer for each of the gases in and out of the bubble through the gas and water interface:

$$\frac{dN}{dt}=K4\pi r^2(C_{gas}-\frac{P_{b_{gas}}}{H_{gas}}) \quad [5]$$

where K is the overall exchange constant for water molecules on a gas phase basis, C_{gas} is the aqueous concentration of the fluid surrounding the bubble, and $\frac{P_{b_{gas}}}{H_{gas}}$ or, C_g, is the concentration of the gas away from the interface at equilibrium. This is effectively a function of the aqueous concentration of the gas, C_{gas}, the gas pressure, $P_{b_{gas}}$, and Henry's Law, H_{gas}. This transfer rate affects bubble size either positively or negatively, where if the concentration of gas in the bubble is much higher than the exterior aqueous concentration, the bubble will degas into the water at a higher rate and the bubble size will decrease as it rises. Gases which are higher in aqueous concentration in the surrounding water, such as nitrogen and oxygen, will cause mass transfer of these gases into the bubble. Nitrogen is well mixed throughout ocean, therefore a constant value based on the partial pressure and Henry's law constant can be used as the maximum aqueous concentration [Gruber 2008]. Oxygen however can vary greatly due to biological and chemical factors. The aqueous concentration of gases, in addition to the salinity and temperature of the surrounding water, are important influences on the bubble dissolution model. Running the

McGinnis model for simulated bubble sizes at an estimated depth of 80m results in Figures 1 and 2. Figure 1 shows the output estimated radii of each different gas released from this depth. These sizes are based on the dissolution rates, where the changing concentrations of each are considered. The molar fractions of each gas for each bubble size as they change throughout the water column are shown in Figure 2.

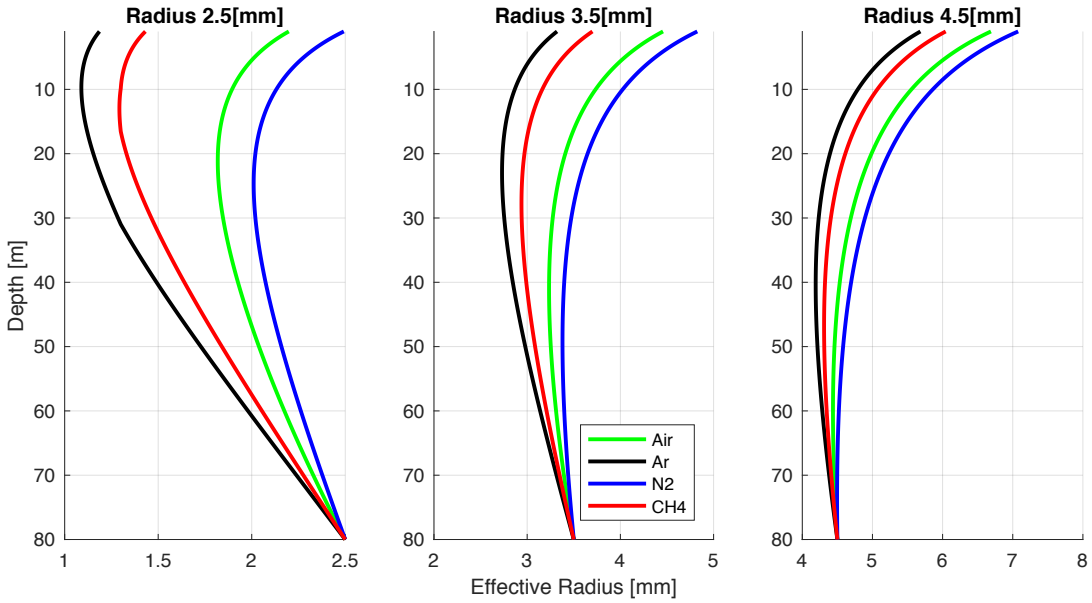

Figure 1: Simulated bubble size evolution of three bubble sizes for each of gas, air, argon, nitrogen, methane.

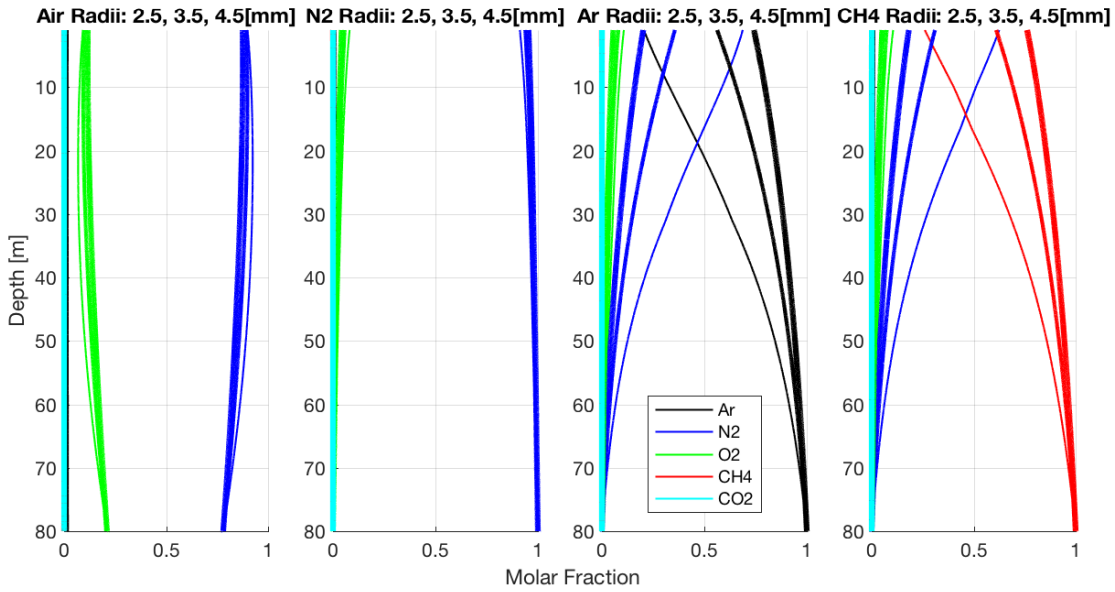

Figure 2: Simulated molar fractions of each bubble after release from an estimated depth of 80[m]. The molar fraction of Argon decreases at a similar rate to methane. This makes argon, and its dissolution through the water column, an appropriate surrogate for methane.

The overall gas transfer rate over the gas-water interface, K, assumes that the bubble surface is clean. More realistically, the surface of these bubbles may be coated with small particles or surfactants, oils, or hydrates which can impact the mass transfer across the surface. These surfactants and coatings can limit the exchange between the water and bubble in addition to altering the surface tension and flow conditions as a bubble rises. Prior studies evaluated this assumption though examination of different gas transfer rates and suggested that the K constant may not be correct [Johnson and Cooke 1981, Weber et al. 2005]. The velocity of a bubble as it rises is also slowed by these surfactants where clean bubbles rise faster than dirty bubbles [Leifer and Wilson 2004]. Testing the sensitivity of the model to local aqueous concentrations of oxygen was performed by running the McGinnis model for anoxic and saturated environments. Using minimum and maximum measured oxygen values for the local environment from the World Ocean Atlas database, the deviation from the model was less than 0.04mm when averaged over depth and

bubble size. The Texas A&M Oilspill Calculator(TAMOC) model, developed by Socolofsky et al. (2015), has a similar estimation method for bubble evolution. Running both models for the example bubble sizes resulted in agreement with a difference of less than 0.002mm when averaged over depth. Considering the impact of these variables, and the unknown level of impact on the models provides motivation to test these assumptions directly.

ii. Acoustic Target Strength

Gaseous bubbles are much more compressible than the water which surrounds them. Acoustically, this results in a larger scattered amplitude compared to a non-compressible sphere due to the ringing of the bubble-water system. The sound impinging on a bubble in the far field can be approximated as a plane wave, where the scattering from a single bubble is omnidirectional. This is illustrated in Figure 3. The incident pressure wave is given by equation 6:

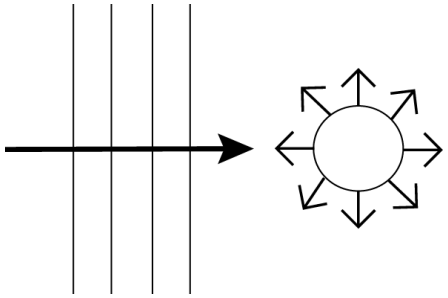

Figure 3: Incident plane wave, and spherical scattering diagram

$$P_i = Ae^{i\omega t} \quad [6]$$

where P_i is the pressure and A is the amplitude of the wave, ω is the radial frequency, and t is time. As this wave interacts with the bubble, the sound is reradiated, scattering spherically. This assumption of spherical symmetry holds true if the ensonifying wavelength is larger than the bubble where ka<<1. Figure 4 illustrates the ka value for a range of frequencies and bubble sizes:

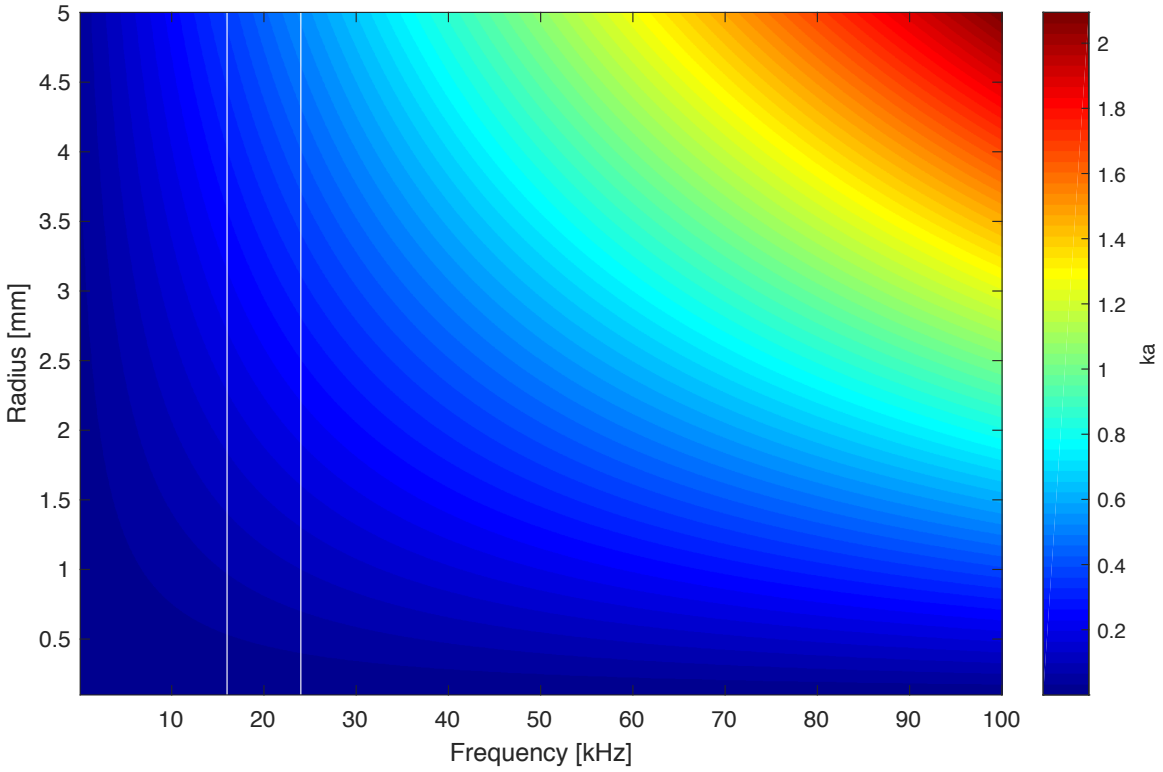

Figure 4: Values of ka for 0.1-100kHz and bubble radii of 0.1-5mm. Vertical white lines denote the effective bandwidth of the ES18, 16-24kHz.

The ES18 transducer used in the field measurements of this study and will be discussed in detail in later sections. The ES18 operates in the bandwidth between 16-24kHz. The white lines in Figure 4 highlight 8kHz bandwidth, and visualize that this assumption is true for most of these bubble sizes at these frequencies. The scattered wave from the bubble received by the transducer is only in the direction which is radially opposite to the incident wave. The backscattering cross-section, σ_{bs}, of a single bubble in the radial direction has been derived resulting in equation 7 [Clay and Medwin 1977]:

$$\sigma_{bs} = \frac{a^2}{\left[\left({}^{fr}/_{f}\right)^2 - 1\right]^2 + \delta^2} \qquad [7]$$

where f_R, is the resonant or natural frequency, f is the center frequency of the FM pulse, a is the bubble radius, and δ is the damping constant from losses due to reradiating, thermal conductivity, and shear viscosity. Converting the backscattering cross-section to target strength in decibels is accomplished using equation 8:

$$TS = 10log10(\sigma_{bs}) \quad [8]$$

where TS is the target strength of a single bubble with a backscattering cross section defined in equation 7. Inverting equation 8 yields an estimate of the size of a bubble from the acoustic target strength measured in the field. The gas composition and environmental parameters also effect target strength. The resonant frequency is shifted, given by equation 9:

$$f_R = \frac{1}{2\pi a}\left(\frac{3\gamma b\beta P_A}{\rho_A}\right)^{1/2} \quad [9]$$

where the a is the radius of the assumed spherical bubble, P_A is the exterior hydrostatic pressure, γ is the effective ratio of specific heats, and where b and β are constants. These are given below in equations 8-10 and are mainly based on the properties of the gas. b and d are real diensionless numbers that account for the change in magnitude and phase of γ.

$$b = \left[1 + \left(\frac{d}{b}\right)^2\right]^{-1}\left[1 + \frac{3\gamma-1}{X}\frac{\sinh(X)-\sin(X)}{\cosh(X)-\cos(X)}\right]^{-1} \quad [10]$$

$$\beta = 1 + \frac{2\tau}{P_A a}\left(1 - \frac{1}{3\gamma b}\right) \quad [11]$$

$$X = a\left(\frac{2\omega\rho_g C_g}{K_g}\right)^{1/2} \quad [12]$$

Where ρ_g, C_g, K_g, are the density, specific heat, and thermal conductivity of the gas respectively. Using equations 7-12, for three bubbles of various gas compositions, the target strength curves are calculated and shown in Figure 5:

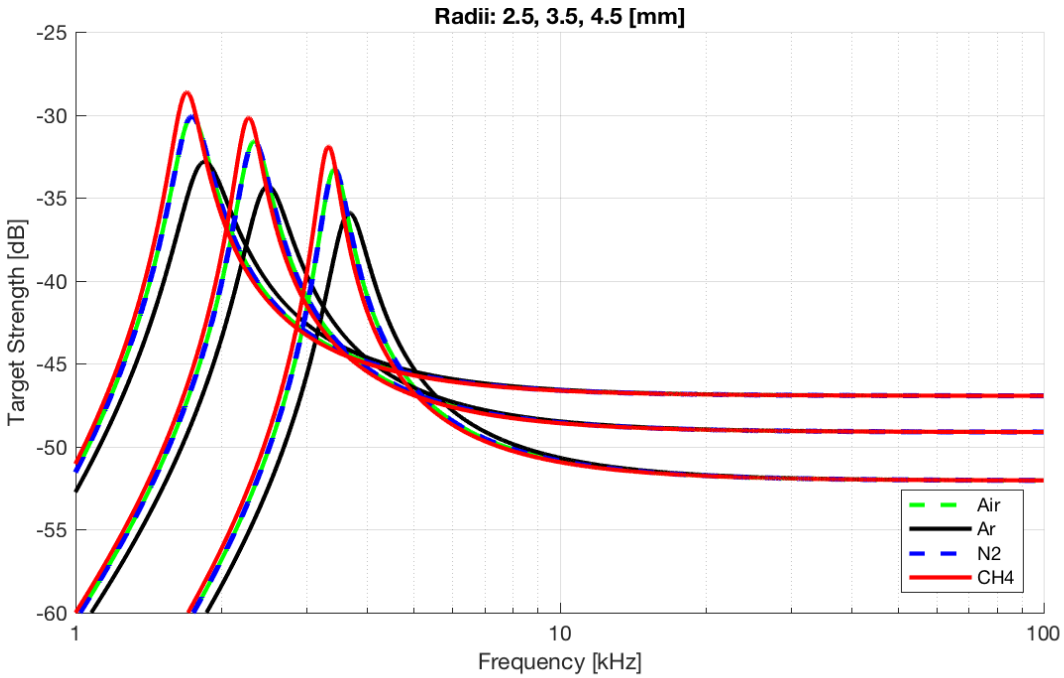

Figure 5: Simulated target strength of three example bubble sizes and differing gas compositions.

The peaks in Figure 5 occur at resonant frequency, and vary in amplitude and frequency based on the bubble's size, gas composition, and depth. The effective radius strongly influences the location and amplitude of the resonance response, where the gas composition among these gasses contributes less. At higher frequencies, above resonance, these curves are near constant, without much variance. These relationships between frequency and target strength show the amplitude of these gasses at 80m depth, however natural gas seeps are composed of variously sized bubbles with changing gas composition as the bubbles rise through the water column. Using the output

from the evolution model from Figures 1 and 2, and calculating the frequency responses for these bubble sizes and gasses for a transducer with 10 to 100kHz results in Figure 6:

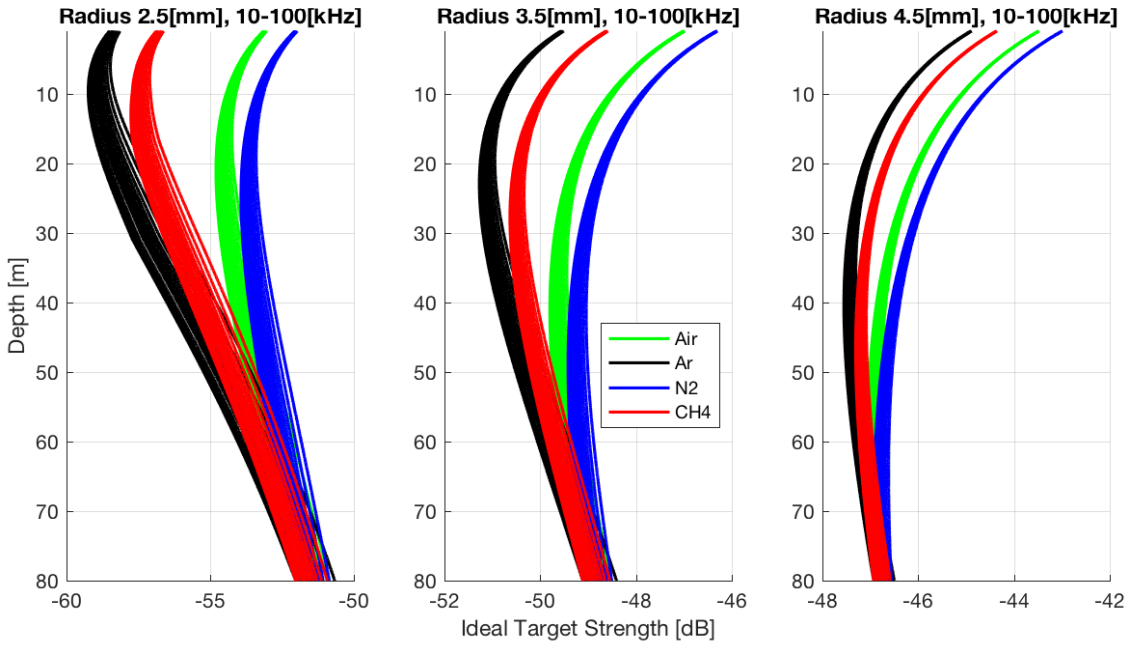

Figure 6: Simulated target strength of three example bubble sizes for air, argon, nitrogen, and methane. Note that these plots are very similar, without much differentiation between the frequencies. The broadband signal is used here for increased resolution rather than detect differences in target strength due to the resonance peak of these bubbles.

where each individual line is the target strength curve for an integer frequency in kilohertz. While many of these target strength curves are relatively close, within a few dB of each other, argon is the weakest, and nitrogen is the strongest. Choosing these two gasses allowed for a direct test by providing the greatest chance of observing this difference in dissolution rates predicted by the model. Argon has a similar dissolution rate to methane due mainly to their relatively low aqueous concentrations. Argon is an appropriate surrogate for methane, and used ultimately to verify the flux rates from the Methane dissolution models. It would be ideal to separate bubbles of these sizes if they were stimulated at or close to their resonant frequency. While a lower frequency system was used to do this, ultimately the SNR was not high enough. Alternatively, with the 16-24kHz

system used, it would be possible to observe the resonance of much smaller bubbles, which have a higher natural frequency.

Central to the analysis employing this target strength model is an assumption of spherical bubbles. Throughout the derivation of equation 7 in Clay and Medwin (1977), there are several solutions employed which are true for perfectly spherical bubbles, but would be more complicated for ellipsoidal or lens shaped bubbles. One such occurrence is the spherical integration of the pressure around the scatterer, where if lens shaped, this wave would be non-uniform over the spherical surface integrated over. Another instance is in the pressure equalization between the inner gas and exterior water, again would not be spherically symmetric. In the result, equation 7, a is the radius for a spherical bubble, however bubbles in the range of 1-5mm are ellipsoidal or lens shaped and have radii which depend on the orientation and shape, changing over time as they wobble. The interface, the surface of the bubble between the gas and water, is assumed clean, and does not account for particles, oils, or hydrates, all of which could affect the acoustic properties and subsequent underlying assumptions for resonance. If there were a coating, consider a shell of oil or a more rigid hydrate, the damping and acoustic properties of the system would be modified drastically. The assumptions made here are worth testing by creating bubbles of known size in the naturally observed range and comparing the measured target strength to the expected value.

III. Seep Generator

i. Design and Construction

A synthetic seep generator has been constructed to facilitate the studies of bubbles similar to those found in natural gas seeps. The seep creates individual bubbles of known size, composition, and flux at depth. The main purpose of this work is to verify the method for methane flux estimation from natural seeps in the ocean. This is accomplished through mathematical models converting the acoustic target strength of individual bubbles to estimates for the total volume of methane from seeps. Bubbles from methane seeps are most commonly found in the range of 1-5mm in effective radius [Leifer and MacDonald 2003, Römer et al. 2012, Weber et al. 2014, Wang et al. 2016]. The synthetic seep, with the current orifice size of 0.79mm, can create bubbles in this range of effective radii at almost any rate, from 0-10Hz. The standard SCUBA tank used as a gas supply for the synthetic seep has a volume of 100c.f. or 2831L. Operating the system at a depth of 100m, this tank of air at 3000psi would be a large enough to generate 8.83×10^8 bubbles of 2.5mm effective radii. This number depends on the depth, size, and cadence of bubbles created, however operationally the current battery bank and gas supply are large enough to create bubbles for at least 1 full day of operation without charging or refilling. While air is available from a SCUBA fill compressor station at pressures up to 3000psi, currently argon and nitrogen are limited to 2400psi as this is the available pressure from the tanks supplied by AirGas. This is an additional limitation on the number of bubbles which can be created from a single tank of these gases. Without additional modifications to the software the current deepest operating depth of the synthetic seep is 130m. With some additional safety precautions added to the code, this depth can be extended to

200m. The lower limit is due to the proof pressure, or maximum differential pressure, rating on the OMEGA differential pressure sensor which is 4 times its range. Since this component has a range of 0-50psi, the maximum pressure which can be applied to the high-pressure side is 200psi. The 200m depth limit is defined by the manufacturer rating on the 1st stage SCUBA regulator from Poseidon. Figure 7 shows the fully assembled system during transit on the back deck the RV Gulf Surveyor.

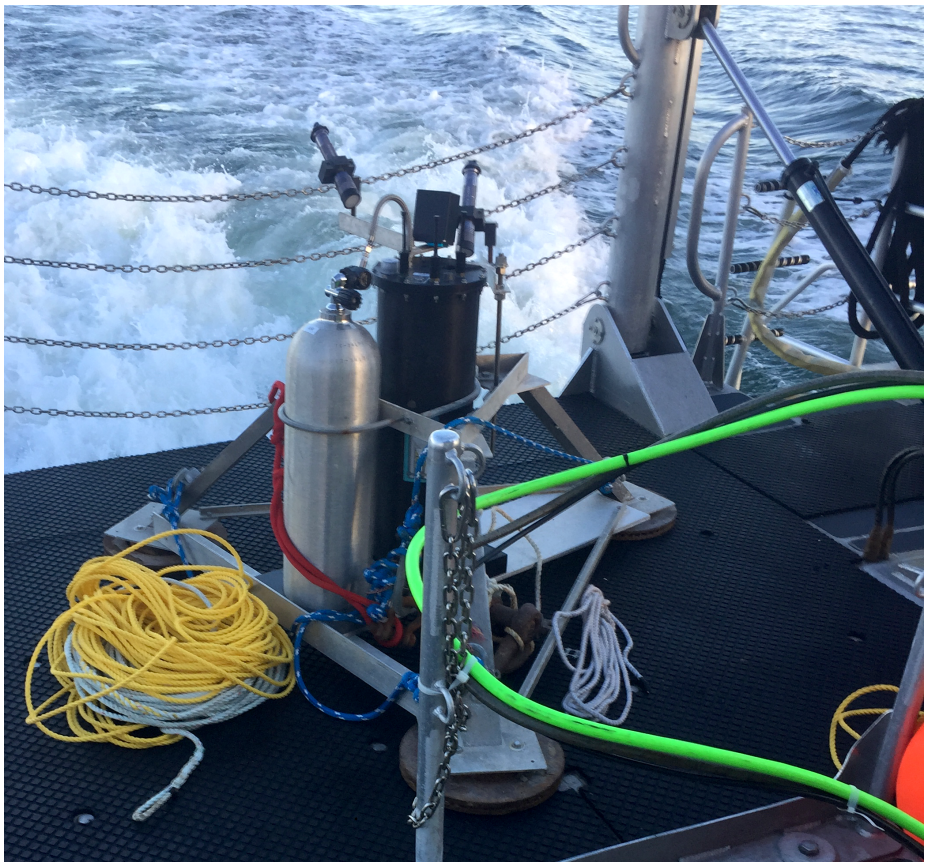

Figure 7: Final bubble maker assembly on board the RV Gulf Surveyor

Individual bubbles are created by energizing a gas injection solenoid valve using a single 4ms pulse. The size of the bubble created depends on the pressure difference across the exhaust port of this solenoid, and the orifice size. The current orifice of the solenoid valve is 0.79mm, however

for smaller or larger bubble sizes, near identical solenoids are available from Parker in a range of diameters from 0.04-0.99mm. The internal pressure of the system is controlled by a Parker miniature calibrant solenoid valve. This valve can be opened for 4 to 10s of milliseconds. To pressurize the system accurately however, the minimum time of 4ms for a single pulse is used while the differential pressure is monitored continuously during this pressurization. To increase the accuracy of the internal pressure, an additional reservoir is used to increase the internal volume. This allows multiple firings of the calibrant solenoid until the prescribed pressure is reached, avoiding pressure overshot. The inlet pressure to this solenoid is controlled upstream by the first stage SCUBA balanced regulator, which reduces the ~200-3000psi from the SCUBA tank to 150psi over ambient, regardless of depth. The differential pressure is measured by an OMEGA pressure transducer which has an accuracy of 0.08% times its range of 50psi, (±0.04psi). This is a stainless wet/wet sensor, meaning that either port can be exposed to water. In the synthetic seep, high-pressure side port is connected to the internal pressure and the low-pressure side is connected to water outside of the housing, or the ambient hydrostatic pressure. The range of differential pressures used to create bubbles is limited by this sensor between 0.1-49.9psi, however for this experiment bubbles were created using 1-30psi. A diagram of this pressure system, control electronics, and associated hardware is shown in Figure 8.

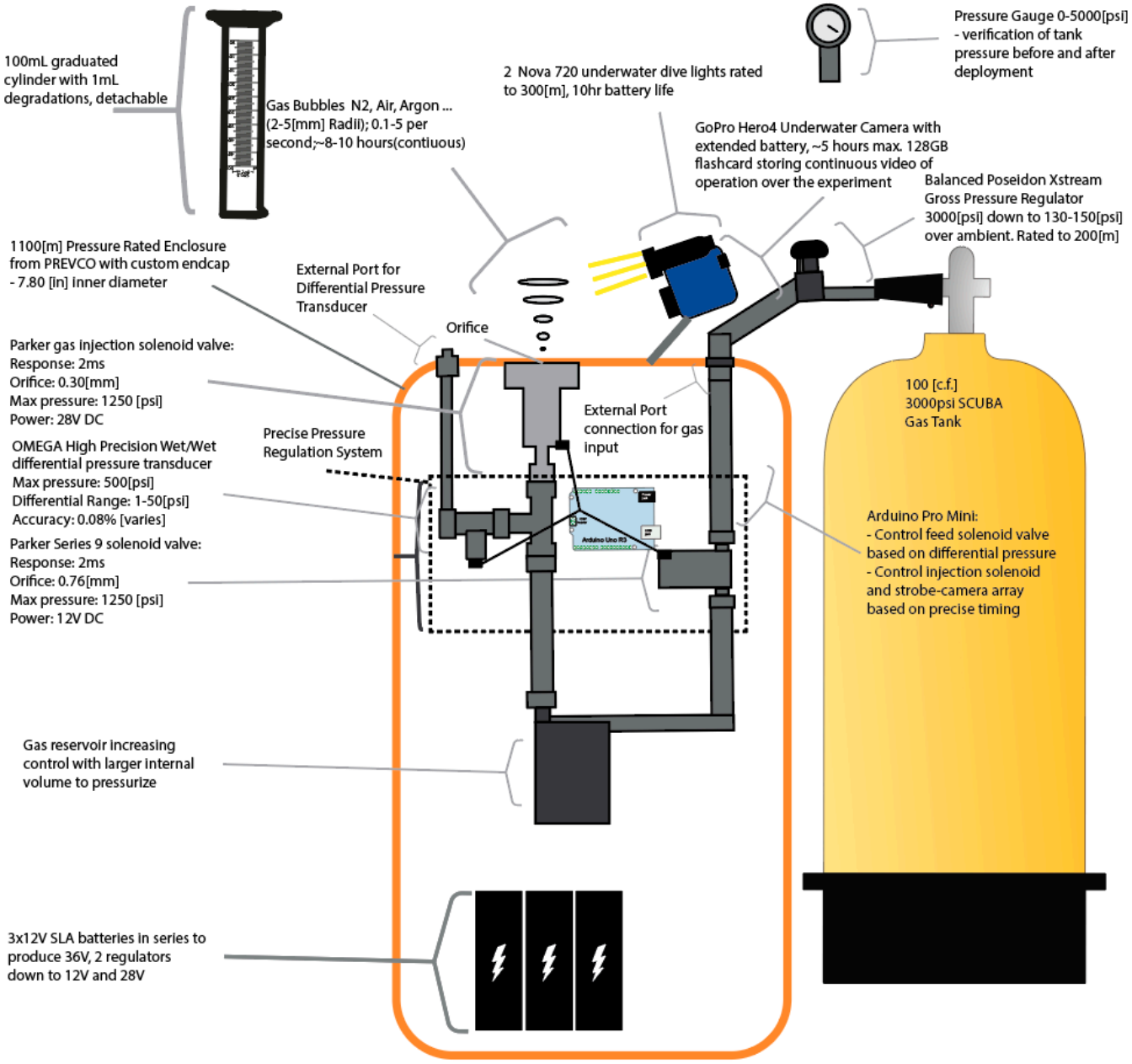

Figure 8: Schematic of the synthetic seep generation system

Control of the synthetic seep is accomplished primarily by employing an Arduino Pro Mini. This small footprint, low power microcontroller is communicated with via serial TTL/FTDI through the endcap. The solenoids are fired by using two N-channel MOSFETs connected between DC voltage regulators and digital pins on the Arduino. When the pin of the Arduino is set to high, 5V is applied

to the gate of either MOSFET, and the supply voltage is applied to the solenoid, energizing it. The amount of time either solenoid is open for is controlled directly by the number of milliseconds set in the Arduino code. The Arduino codes used to operate the synthetic seep are included in Appendix B. The OMEGA differential pressure sensor has an output of 0-5V, corresponding to its range of 0-50psi. This output is read directly by the analog input of the Arduino and converted into pressure in psi based on the 10-bit analog to digital conversion and the calibrated range of the sensor. The pressure threshold with which a bubble is released is set in the Arduino code before deployment, or based on a timer loop though the use of scripting. Using this programmatic timing alleviated the need for multiple deployments if multiple bubble sizes were required at once. The threshold is compared to the differential pressure reading before and after firing the calibrant solenoid, to determine whether the internal pressure is above the threshold. If the system pressure remains below threshold, the calibrant solenoid will be energized in a loop until the threshold is reached. Before the exhaust solenoid is fired, the pressure difference is checked once again as a safety to verify that the difference is positive and that backflow will not occur. This pressurization between bubbles occurs within a matter of milliseconds, depending on the size of the bubble and the pressures involved. Figure 9 details the electrical control circuit in the synthetic seep.

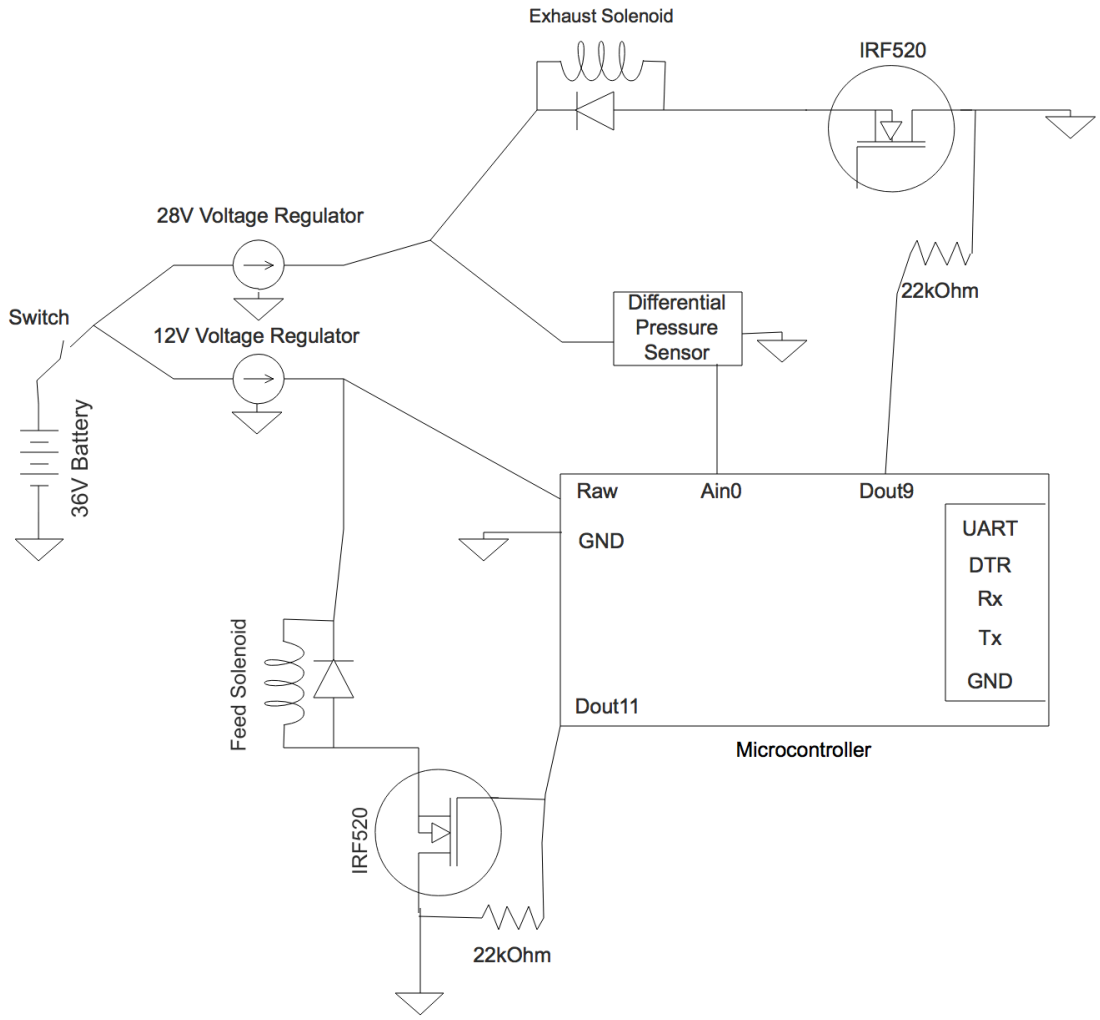

Figure 9: Electrical diagram for pressure control and operation of synthetic seep. Note that there is a leak probe included as a separate measure to detect small leaks in the housing.

The size of the bubble is determined by the output volume flow rate of the fluid through the orifice and the time the solenoid is open. This rate is dependent on the environmental conditions, mainly the ratio between the internal and external pressure and the size of the orifice. A model of this system was derived by Sanville (1971), and has been updated over time [Beater 2007, MatLab 2009, ISO6358-3 2014]. This model is valid for pneumatic fluid flow for compressible gasses through an orifice of fixed size with sharp edges in a steady state. Equation 13 shows the

relationship between the environmental parameters for three separate regions depending on the expected exit velocity of the gas. Figure 10 illustrates these regions over the operating depths and differential pressures of the bubble maker.

$$V = \begin{cases} k \cdot p_i \left(1 - \frac{p_o}{p_i}\right) \sqrt{\frac{T_{ref}}{T_i}} \cdot sign(p_i - p_o)/\rho_o & if\ \frac{p_o}{p_i} > \beta_{lam}\ (laminar) \\ p_i \cdot C \cdot \rho_{ref} \sqrt{\frac{T_{ref}}{T_i}} \sqrt{1 - \left(\frac{\frac{p_o}{p_i} - b}{1-b}\right)^2} \Big/ \rho_o & if \beta_{lam} > \frac{p_o}{p_i} > b\ (subsonic) \\ p_i \cdot C \cdot \rho_{ref} \sqrt{\frac{T_{ref}}{T_i}} / \rho_o & if\ \frac{p_o}{p_i} \leq b\ (choked) \end{cases} \quad [13]$$

$$k = \frac{1}{1-\beta_{lam}} \cdot C \cdot \rho_{ref} \sqrt{1 - \left(\frac{\beta_{lam} - b}{1-b}\right)^2}$$

V is the volume flow rate, k is a gain constant defined above, p_i is the internal pressure, p_o is the external ambient hydrostatic pressure, T_{ref} is the temperature at which the sonic conductance was measured (T_{ref} = 293.15 [K]), T_i and T_o are the inlet and outlet temperatures respectively, ρ_{ref} is the gas density at which the sonic conductance was measured (1.185 [kg/m^3] for air), $\beta_{lam}$is the pressure ratio at laminar flow, a value between 0.999 and 0.995, $\rho_o$is the density of the bubble in after creation, given by equation 14:

$$\rho_o = \frac{M \cdot p_o}{R \cdot T_o} \quad [14]$$

where M is the molar mass of the gas, and R is the gas constant. The sonic conductance, C, is defined in equation 15, and b is the critical pressure ratio at which the gas achieves sonic speed, shown in equation 16 [Gidlund 1977]:

$$C = 0.128\, d^2 \quad [15]$$

$$b = 0.41 + 0.272\frac{d}{D} \quad [16]$$

where d is the diameter of the solenoid orifice, and D is the diameter of the upstream pipe. The synthetic seep system performance was modeled using equations 13-16. The ratio of inlet to outlet pressure is defined by the differential pressure threshold used when creating the bubble. Figure 10 illustrates this ratio over the effective operating depths of the seep. The three regions of flow are noted at the respective values for critical pressure ratio and laminar flow. Above the critical pressure ratio, the flow is supersonic and becomes choked, where any increase in the rate is dependent on the inlet pressure. Between this ratio, and β_{lam}, the flow is subsonic. This region is where most of the bubbles are created. At very low differential pressures, the flow is laminar. Figure 11 converts the predicted flow into estimated effective radii output based on the differential pressure the bubble is created at and the time the solenoid is open for. The model predicts that at shallow depths the change in the size of the bubble created at one differential pressure varies at a higher rate. This change in bubble size decreases as the depth increases, reducing the discrepancy between size and differential pressure.

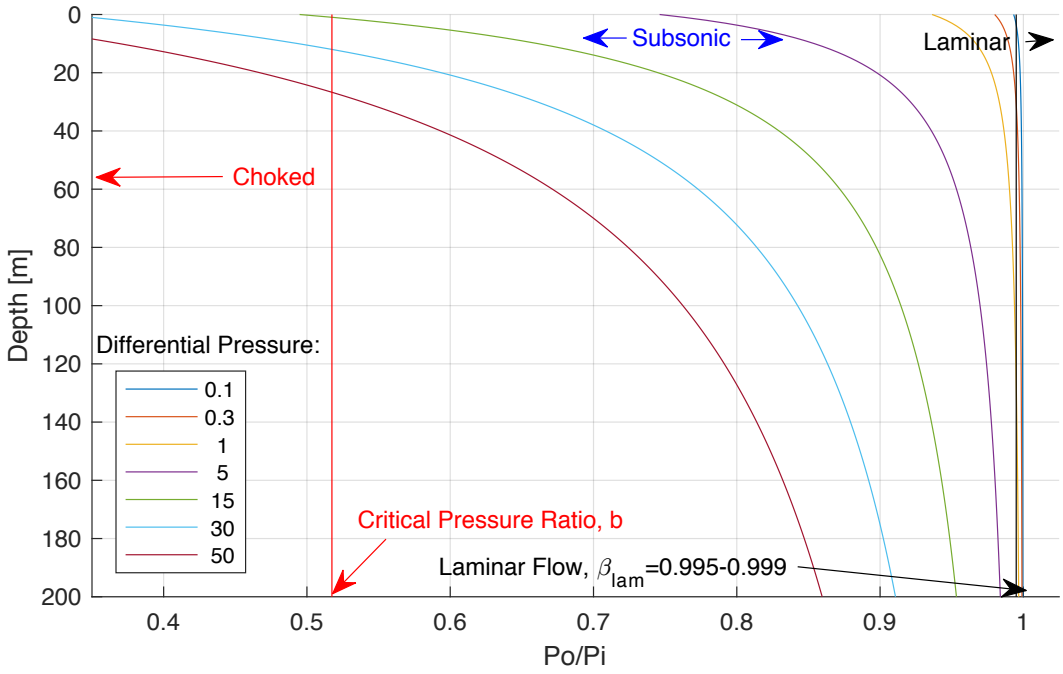

Figure 10: Regions of flow conditions based on pressure ratio, $\frac{p_o}{p_i}$, and depth. Each line represents a separate differential pressure threshold.

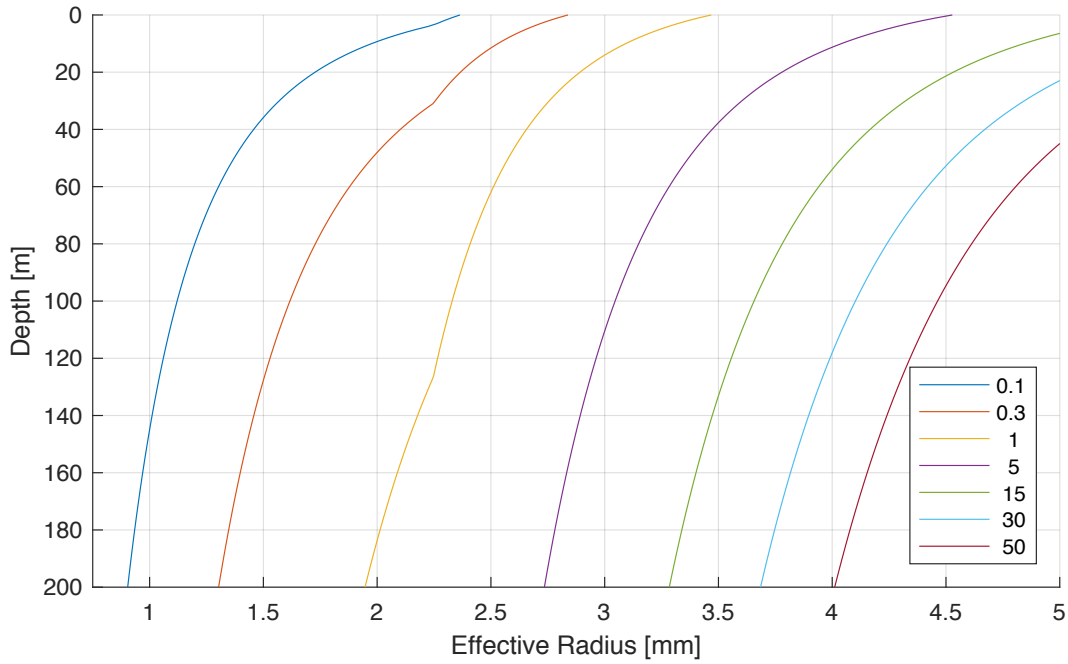

Figure 11: Estimated effective radius of a Nitrogen bubble created over a range of depths at various differential pressures.

This model is valid for steady state; however, the synthetic seep orifice and bubble release system is changing constantly during the single pulse of the solenoid. When the bubble is released, the gas is accelerated and stopped abruptly through the orifice and exit cone, far from the steady state condition. Another assumption this model makes is that the gas flows freely downstream into an identical gas mixture without restriction. In operation however, the orifice dispenses into sea water, which is 3 orders of magnitude denser and much less compressible compared to the gasses injected. Considering these limitations, the model is not completely accurate, however it is useful to have some basic understanding of how the system performance depends on depth.

ii. Bubble Size Calibration

Given the violation of assumptions made in the modeled outputs of the gas injection solenoid, a calibration procedure was developed which can be performed in the tank or in the field. Previous calibrations had been performed in the tank using a machine vision camera system by measuring the size of non-spherical bubbles by estimating the two radii of the ellipsoid, then relating these to the effective radius of an equivalent volume spherical bubble. To simplify and add robustness to this process for a field deployable system, verification of bubble size was achieved using an inverted graduated cylinder above the outlet orifice to directly measure the bubble volume. The calibration was accomplished remotely through video and audio acquired using 2 NovaPro dive lights with diffusors and a GoPro Hero 4 encased in a GroupB underwater housing, both affixed atop the synthetic seep. The volume was calculated by subtracting the level of the water-gas interface before and after filling the cylinder, and counting the number of bubbles created. Figure

12 shows the calibration setup with the graduated cylinder and arrows noting the meniscus levels in the tank(top) and in the field(bottom).

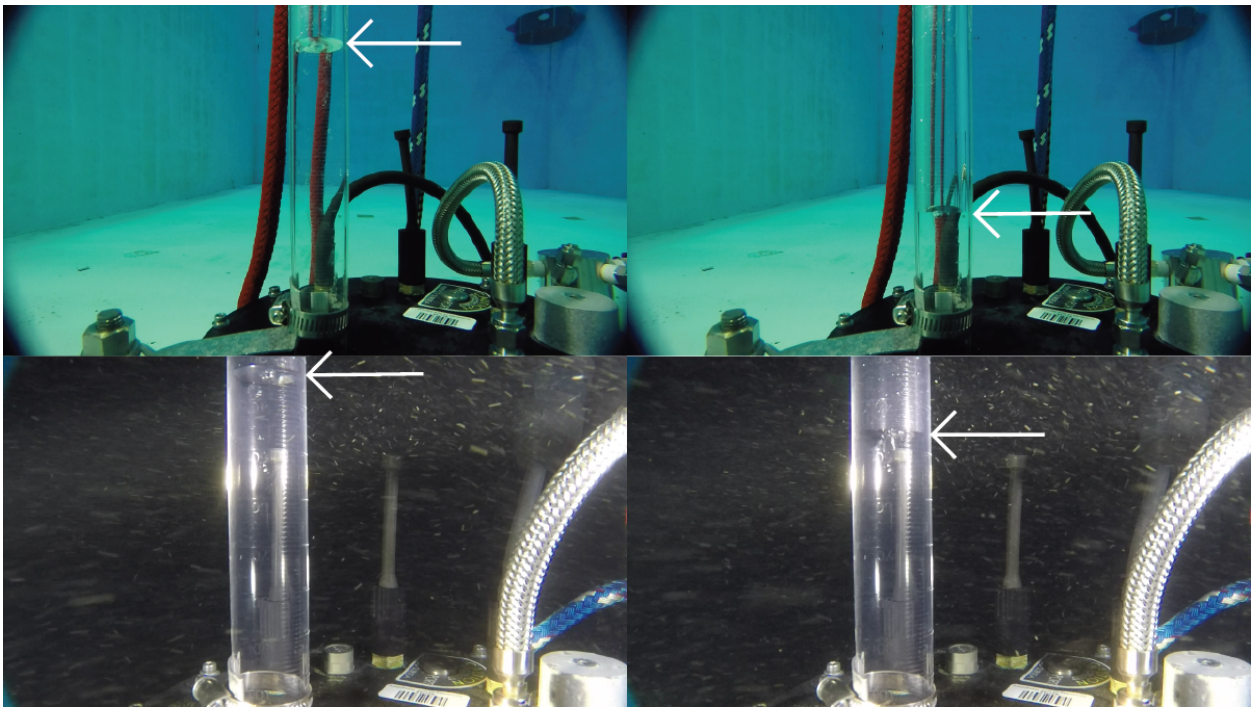

Figure 12: Calibration of bubble size using inverted graduated cylinder acquired in the tank(top) at 5[m], and in the field(bottom) at 60[m]. White arrows mark the meniscus level of the gas in each cylinder, (left) before filling, (right) after.

Counting the bubbles created, measuring the volume on the cylinder's gradations, and accounting for the hydrostatic pressure where the bubbles were created, a consistent bubble volume was achieved given an input differential pressure threshold. Argon, nitrogen, and air gases were used in three 100c.f. Scuba tanks. Each tank was emptied to less than 10^{-4} bar using a vacuum pump removing any gas, then filled to ~2400psi with 99.95% or higher purity N_2 and Ar using a three-stage pressure bank system. To switch the system between gasses, the SCUBA tanks were switched, and a 2-stage purge procedure was carried out. The two stages of the internal pressure system were pressurized and vented downstream so that the bubbles created by the seep contained

99%+ concentration of the desired gas. This was accomplished first by pressurizing between the SCUBA pressure regulator and calibrant solenoid and venting at least three times. In practice this was performed five times, each to 150psi, by manually opening and closing the Yor-Lok connection on the end cap. This ensured the first stage of the pressure system was highly concentrated with the desired gas. The internal pressure system of the synthetic seep was purged through a similar procedure by manually controlling the solenoids through the Arduino software. First the calibrant solenoid pressurized the system while reading the output of the differential pressure sensor, then the exhaust solenoid was fired, venting gas until this pressure differential was nearly zero. This was repeated a minimum of three times, in practice five. The calibration procedure was tested in the tank and in the field using all three gasses, and was repeated at depth for the specific bubble sizes measured acoustically in the field. Figure 13 shows the calibration results from the various differential pressure thresholds and the output effective radii of the bubbles generated.

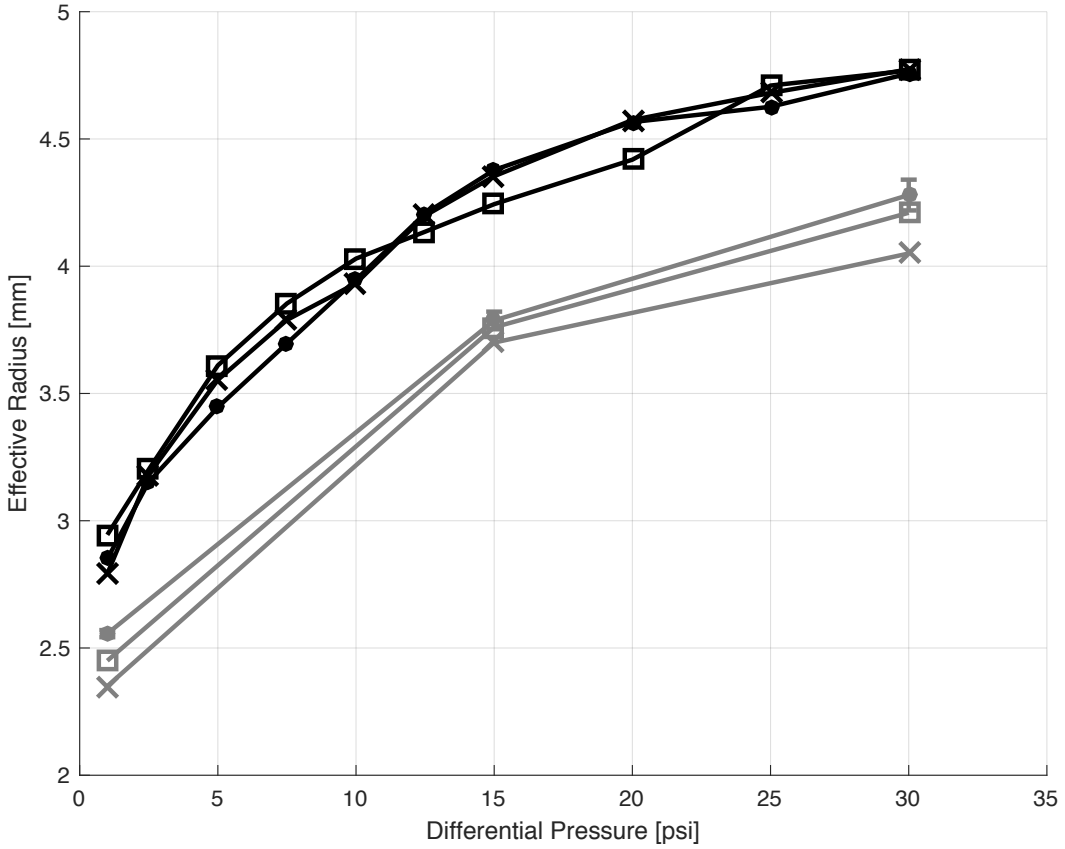

Figure 13: Differential pressure vs. bubble size calibration, black denotes a tank calibration while grey denotes field calibrations in an order of magnitude greater depth. Air uses a dot marker, nitrogen uses a square, and argon uses an x. Note that the air calibration in the field was done at a different time and location as an independent study. The error bars from this study are the standard error from a single measurement of each size bubble. The N2 and Ar curves were the final field calibrations completed on the day of acoustic data collection.

The difference between the tank and field calibrations is expected based on the output of the modeled volume flow for this system as shown in equation 13 and illustrated in Figure 11. Ultimately the bubble sizes from the field calibration on the day of data collection are used to align the dissolution models with the acoustic data.

IV. Field Tests

i. Overview of Experiment

In order to test the assumptions in the models for the evolution and acoustic response of bubbles, the synthetic seep was deployed at sea and the acoustic backscatter was measured with calibrated sonar. The bubble maker described in the previous sections created acoustic targets of known size and gas composition in the water column. This was accomplished by mobilizing the bubble maker tripod and an acoustic suite aboard the RV Gulf Surveyor (RVGS). The RV Gulf Surveyor was employed for its A-frame, necessary for deploying the tripod, and the acoustic strut and moon pool, which allowed for a battery of acoustic systems to be mounted simultaneously. Mobilization and demobilization were accomplished on separate days prior to and after the experiment. This allowed for flexibility due to weather conditions and maximized the amount of time available in a single day at the deployment site. The deployment site chosen for the synthetic seep was located south west of the Isles of Shoals. This area has a depth of ~60m and is reasonable travel distance, allowing field operations for most of a single day. Alternate locations with similar or greater depths were considered, for instance east or south east of the islands, however these were more exposed depending on the wind direction, and would take a considerably longer amount of time to steam to and from each day. The synthetic seep bubble generator was deployed over two days in October 2017 south of the Isle of Shoals, New Hampshire, as shown in Figure 14.

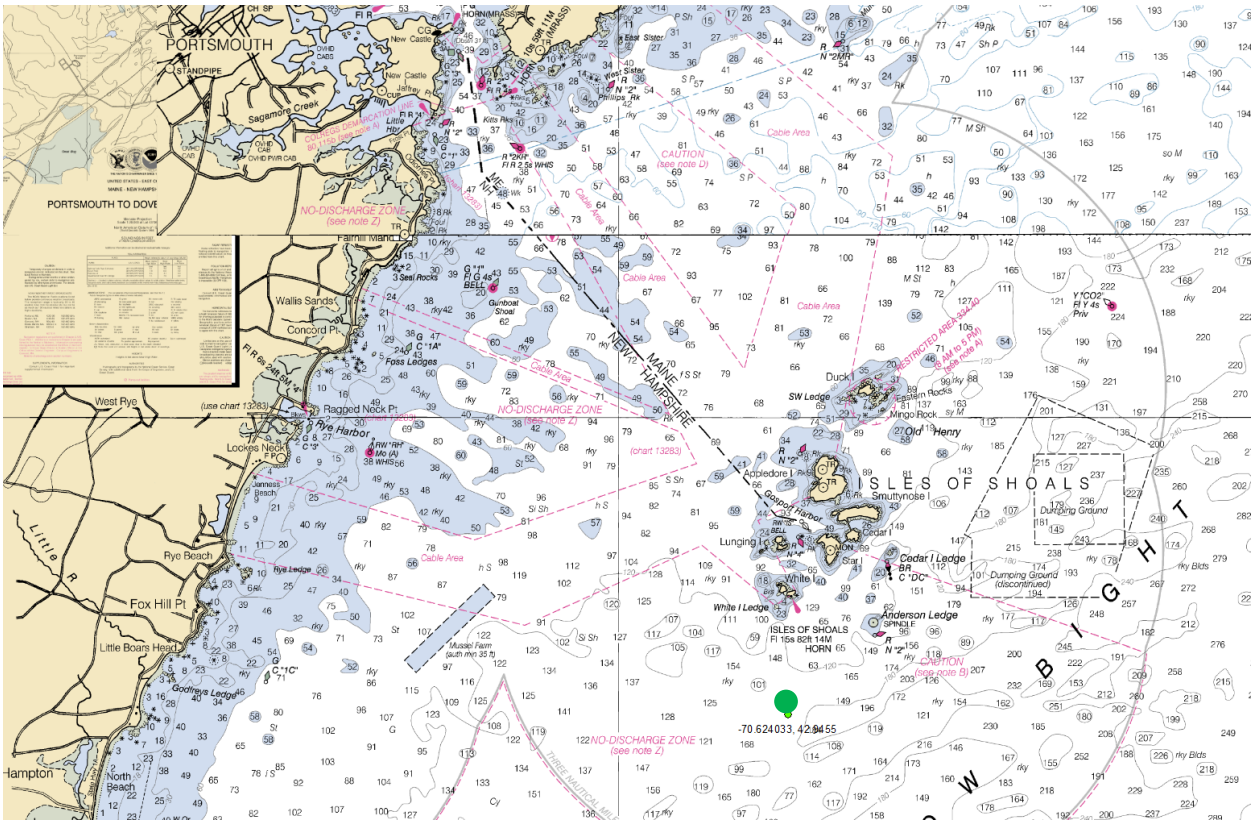

Figure 14: NOAA chart of the experiment area showing depth contours and soundings, the UNH pier and deployment location. This location is marked by green dot at (-70.624033N, 42.9455W), where the artificial seep was deployed, acoustic data was collected, and CTD cast. The depth of the water was ~60[m] south west of the Isles of Shoals.

where the green dot denotes the location of the deployment. The bubble maker deployment was accomplished using a float and weight mooring system shown as a diagram in Figure 15.

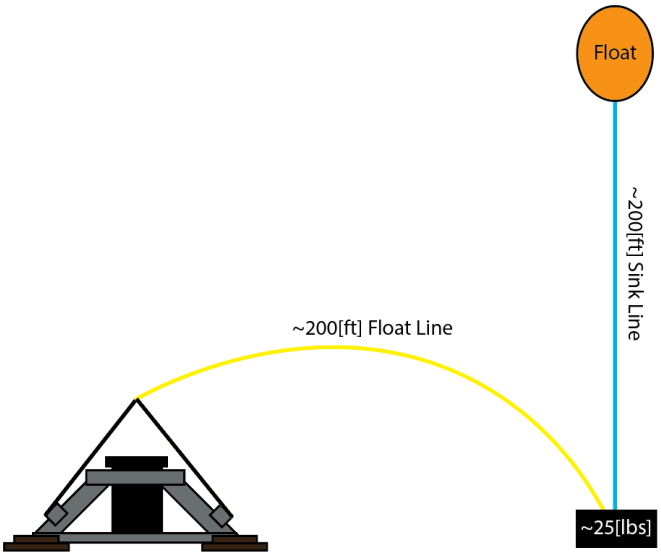

Figure 15: Mooring diagram synthetic seep deployment. Shown are the bubble maker and tripod, float line(yellow), weight, sink line(blue), and floating buoy(orange). Not to scale.

The tripod was attached by a ~200ft float line connected to a set of weights before splicing into ~200ft of sink line and large tufted buoy. This mooring setup was used to remove any line or other mechanical objects which may cause acoustic scatter from the direct path between the bubbles in the water column and the beam of the transducer. By using float line and attaching large shackles as weights during the deployment, the line was 'stretched' out, over the seafloor so that the line which rose vertically through the water column to the buoy would be some distance away from the seep created. The float line was used specifically so that it would not sink down and lie directly on the seafloor, avoiding possible tangling or interference from rocks or other objects.

Bubbles of three sizes of both argon and nitrogen were made over the course of the two days of deployments using the two-stage purging procedure performed onboard the RVGS when switching between gases. To measure the bubbles acoustically, a broadband suite of sonar systems was

assembled and mounted onto a large sled then attached to the strut on the RVGS shown in Figure 16. A Kongsberg ES18 fisheries splitbeam echosounder was employed using the EK80 transceiver and acquisition software. The main results discussed are from the ES18 which has an effective bandwidth covering the 16-24kHz range. Detecting the seep with this transducer in relatively rough seas of ~3ft waves was a complicated task. The ES18 has a beamwidth of ~11 degrees, so in 55m of water, the beam footprint is roughly a 12m diameter circle. Operationally positioning the seep within the beam of the transducer was accomplished by marking the point on the ship's navigation at the exact point the bubble maker hit the bottom, judging this on the mechanical load measured by the hydraulic winch holding the line of the bubble maker. Steaming slowly or drifting the RVGS in a star or grid like pattern across this point yielded multiple realizations of the seeps in the water column. The seep generator was recovered and deployed for each separate size and gas. This allowed data quality to be assessed real-time, ensuring that an adequate amount of data was acquired from each seep.

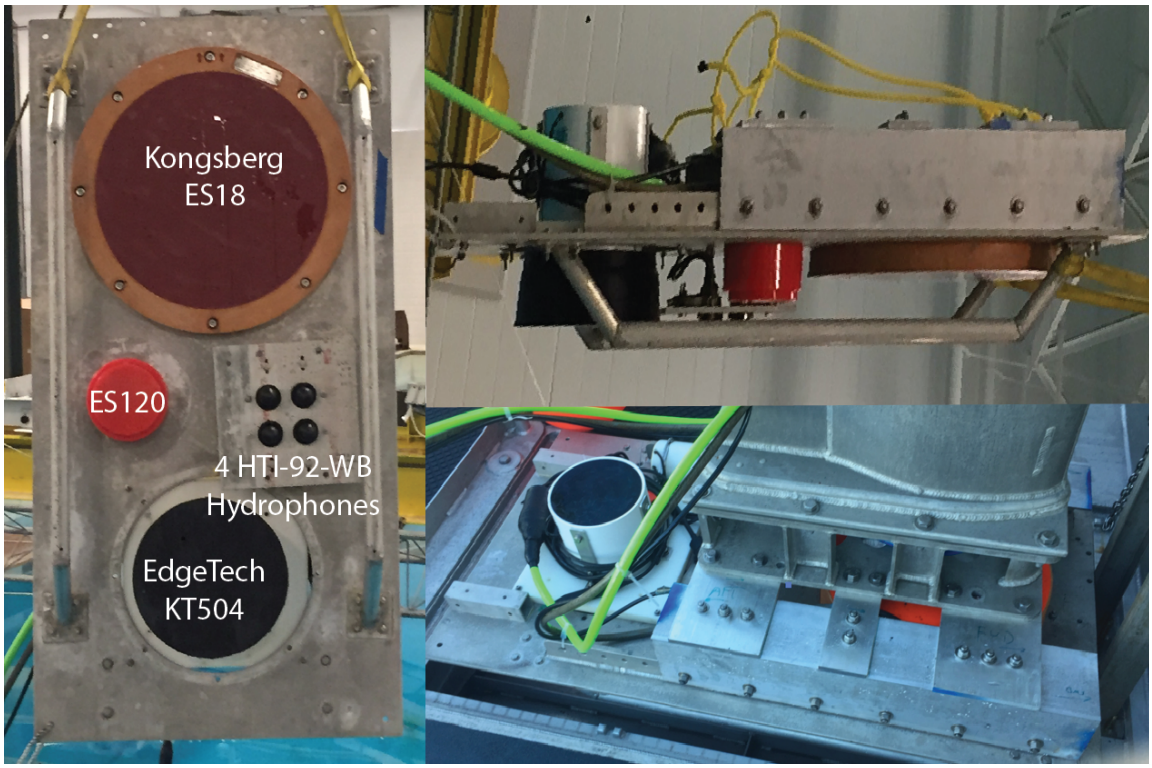

Figure 16: Layout of broadband acoustic suite as affixed to sled, (left) viewed from underneath transducer faces, side view (top right), and as mounted on the main strut aboard RV Gulf Surveyor (bottom right). Results from Kongsberg ES18.

ii. Acoustic Calibration

To convert the signals received from the bubbles in the field to target strength, an acoustic calibration was performed. This calibration accounts for offsets in target strength over the complete beam pattern of the transducer from angularly dependent amplitude variation. This method has been used in prior studies [Foote et al. 1987, Demer et al. 2005, Weber and Ward 2016]. This calibration was performed in the engineering tank at UNH, and while the sonar was mounted on the vessel at sea in the region where the data were collected. For this experiment a full tank calibration was run, in addition to a more limited calibration at sea. The at-sea calibration served as a spot check so that any environmental variables, mainly temperature and salinity, could

be accounted for, ensuring the tank beam pattern calibration was valid for the data collected at sea. To relate back to target strength, objects with a well characterized target strength, a copper or tungsten sphere, are used. The target strength values for these spheres are shown in Figure 17. For this experiment a 64mm copper sphere was used. The mapping of the ES18 transducer's beam pattern was accomplished by moving the sphere physically throughout the entire beam. Each ping ensonifies the sphere in a slightly different location within the beam, corresponding to a range of along track, ϕ_{along}, and across track, $\phi_{athwart}$, angles. The output of this calibration is shown in figure 18, where the correction factor is calculated from the difference between the known target strength of the sphere at the center frequency from Figure 17 at 19kHz, and the measured response at each pair of angles. This correction factor, Cf, is applied to the signal amplitude from observed targets in the water column. The fit in Figure 18 is a two-dimensional quadratic surface, given by equation 17, with coefficients and 95% confidence intervals given in table 1.

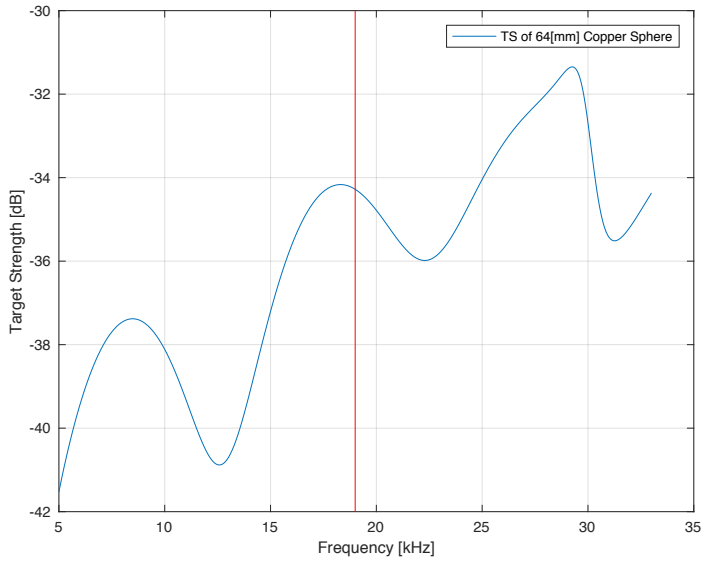

Figure 17: Target strength of 64mm diameter copper sphere used vs. frequency. Vertical red line indicates central frequency, 19kHz. Note there are no distinct nulls from this sphere over the bandwidth of the ES18.

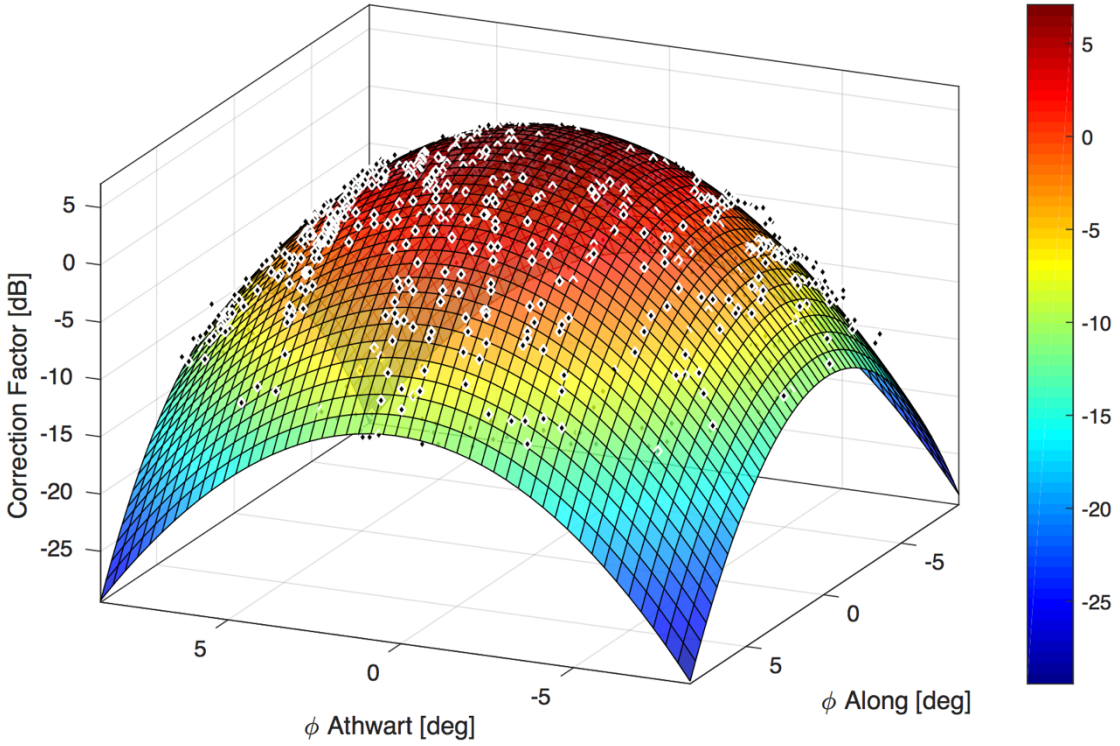

Figure 18: Correction factor from beam pattern calibration, parabolic surface fit for both athwart and along track directions.

$$CF = \mathrm{p00} + \mathrm{p10}\phi_{al} + \mathrm{p01}\phi_{ath} + \mathrm{p20}{\phi_{al}}^2 + \mathrm{p11}\phi_{al}\phi_{ath} + \mathrm{p02}{\phi_{ath}}^2 \qquad [17]$$

Table 1: Coefficients and confidence intervals of two-dimensional quadratic fit:

Coefficient	Value [dB]	Lower 95% CI	Upper 95% CI
p00	7.075	6.949	7.202
p10	0.04937	0.03219	0.06656
p01	-0.04328	-0.06151	-0.02505
p20	-0.2459	-0.2498	-0.2421
p11	0.002909	-0.002268	0.008085
p02	-0.2433	-0.2471	-0.2396

The root mean squared error for this fit is 1.218 with an R^2 value of 0.959. These metrics indicate that data and fit are aligned well. These uncertainty estimates are smaller than the variation seen in the acoustic field data and are not a primary source of uncertainty. Visualizing the calibration data relative to the fit, figure 19 illustrates the residuals where the fit is subtracted. The stems and

color of the point represent the distance from the fit. These residuals are normally distributed about zero, indicating that the beam pattern is correctly accounted for.

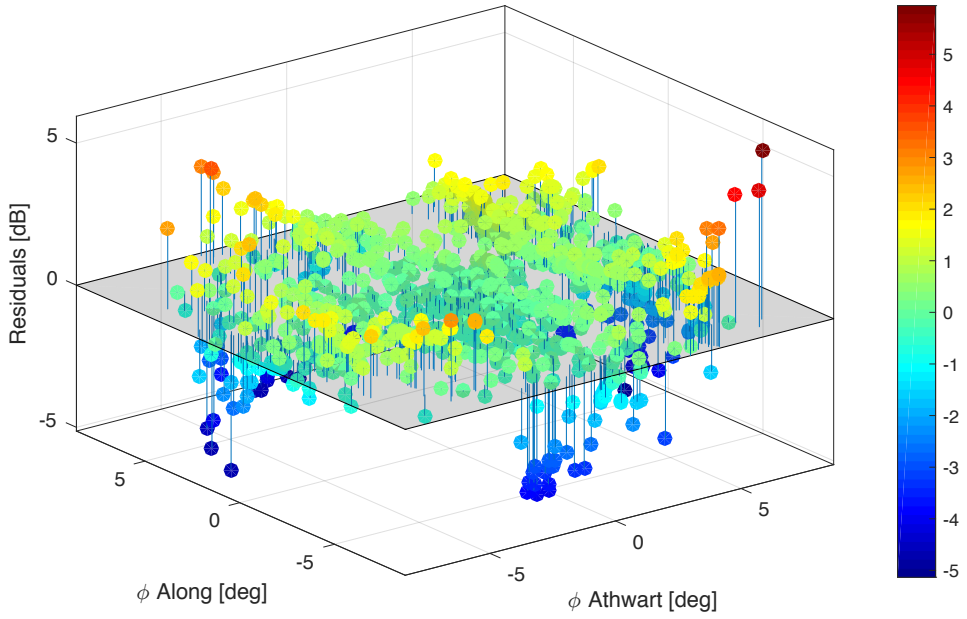

Figure 19: Residuals from the calibration data and 2d quadratic fit in both Athwart and Along track directions.

Using these residuals, the 95% functional confidence bounds are calculated and overlaid on the calibration data in figure 20. However, with the range of the y-axis, it is difficult to visualize these intervals. Figure 21 subtracts the beam pattern, showing the confidence intervals in both angular directions as they deviate from the fit. In this display, is clearer that the confidence interval expands out from the MRA to an extent of approximately 1dB from the fit at 10 degrees. This level of variability from the confidence in the target sphere measurements is much lower than the uncertainty for individual measurements in the experimental results discussed in table 2.

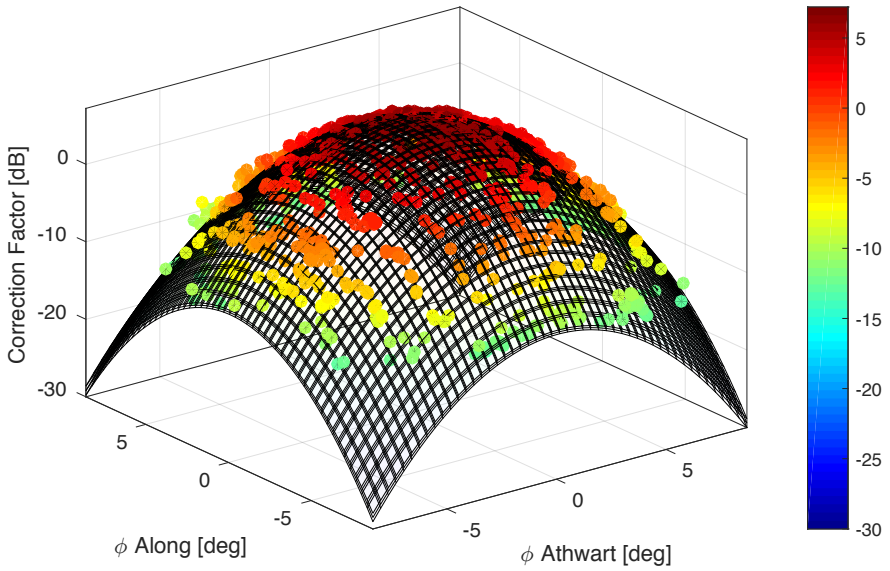

Figure 20: Correction factor, fit, and confidence intervals. Data are colored based on correction factor, fit and functional confidence intervals are overlaid as transparent grid surfaces. Note the intervals are almost too close to the fit to observe visually.

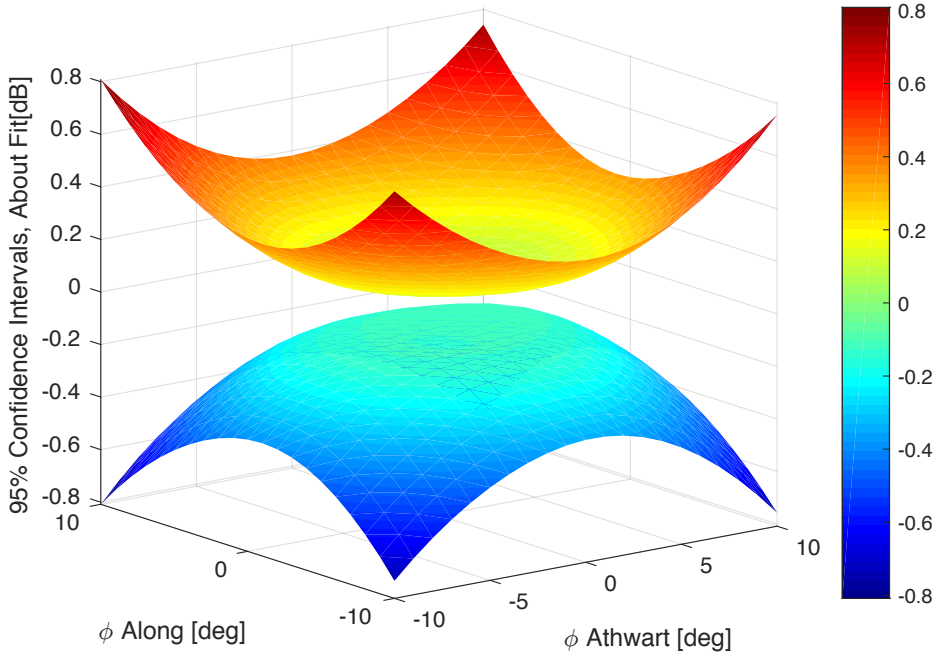

Figure 21: 95% functional confidence intervals subtracting the fit to remove the beam pattern. The increased range of the intervals increases with angle from the MRA.

Another result which this calibration can provide is the performance of the transducer with respect to frequency. Using the signal from the sphere at multiple angles as a sample, it is possible to examine the change in the beam pattern by calculating the Fast Fourier Transform(FFT). Taking the FFT for each frequency and angle, and fitting the result, as shown in Figure 22.

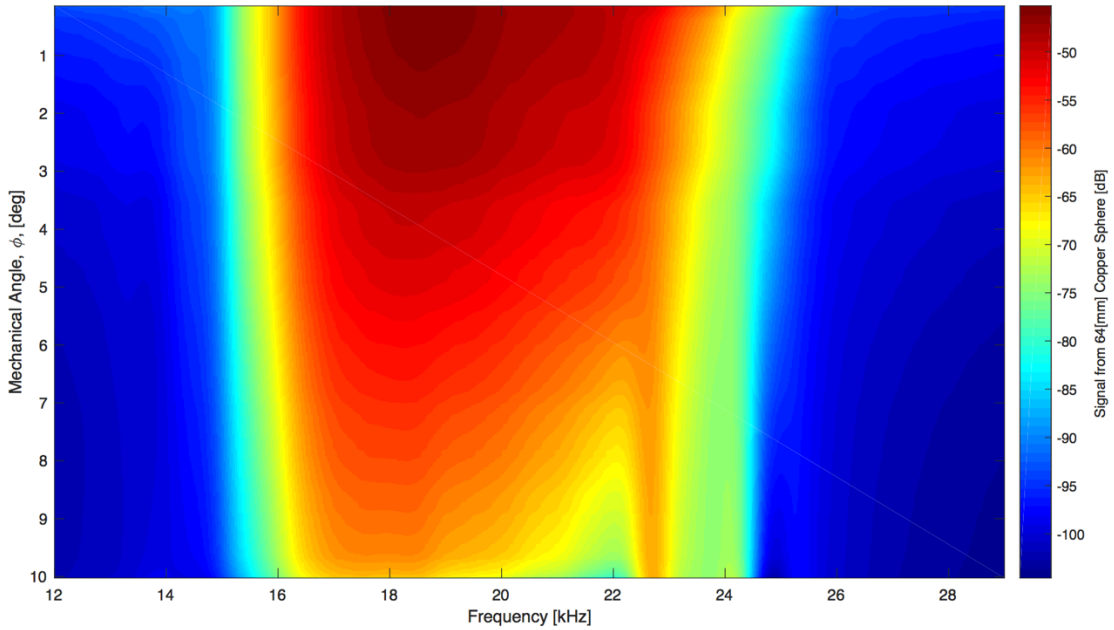

Figure 22: Signal from target sphere at different mechanical angles and frequencies.

where the signal level of the sphere for each mechanical angle and frequency is presented. Although the transmit signal sent to the transducer was wider than 16 to 24kHz, the response in Figure 22 shows that the transducer effectively only produced or received signal within this 8kHz bandwidth. With this knowledge, a bandpass filter with these bounds was applied to the data, removing signals from higher or lower frequencies. The noise from other sources at these frequencies, in the 10s of kHz, are likely from higher frequency data aliased down into this bandwidth.

iii. Overview of Data

A Seabird SBE 19plus V2 CTD with conductivity, temperature, and pressure sensors, was cast once per day through ~50 meters of the water column, resulting in the data shown in Figure 23. These measurements are input as variables into the evolutions models for sound speed, absorption, and the dissolution of the bubbles throughout the water column. The O_2 and N_2 saturation values are inferred from the other CTD measurements by assuming the gases from the atmospheric interface are well mixed, and that the concentration of the water below follows this mixing pattern [Weiss 1970, Seabird 2017]. Prior direct measurements of O_2 were acquired from the World Ocean Atlas, location and data shown in Figure 24. Note this location is 0.13 degrees away from the estimated location, approximately ~6mi, or 10km to the south west of the deployment location near the Isles of Shoals [World Ocean Database, 2015]. The large range in the confidence intervals is likely due to the unfiltered nature of this database since all data are included. The minimum and maximum values from this profile indicate that the sensitivity to aqueous oxygen over the depths in this experiment is less than 0.04mm when averaged over depth and bubble size.

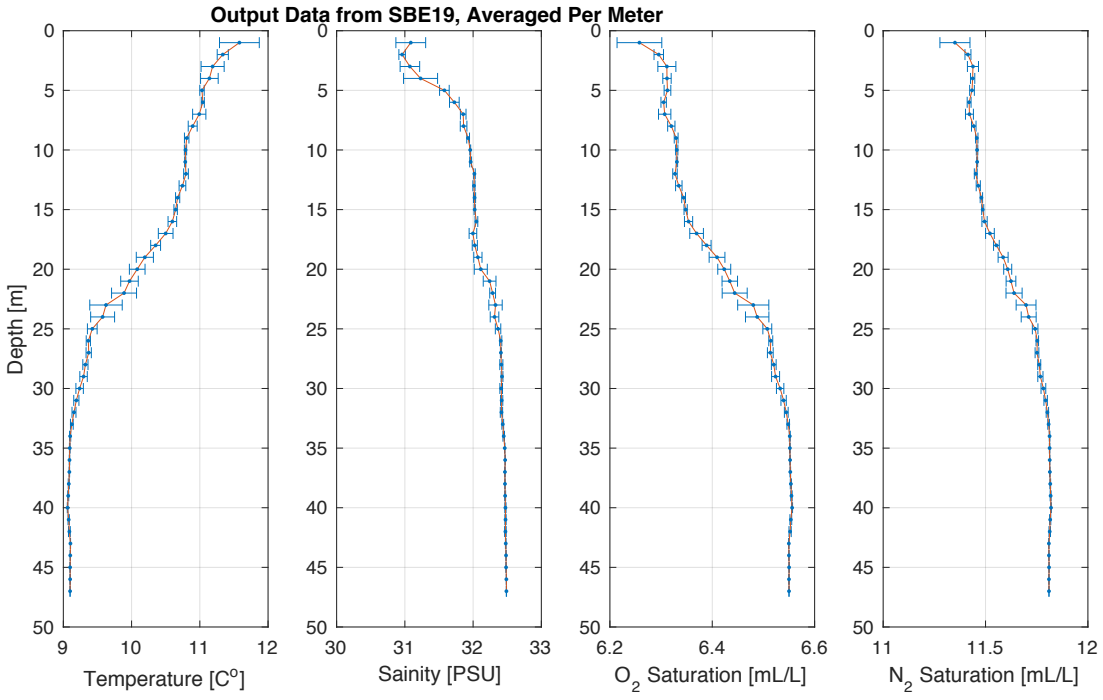

Figure 23: CTD profiles from SBE 19 cast, averaged in 1 meter increments.

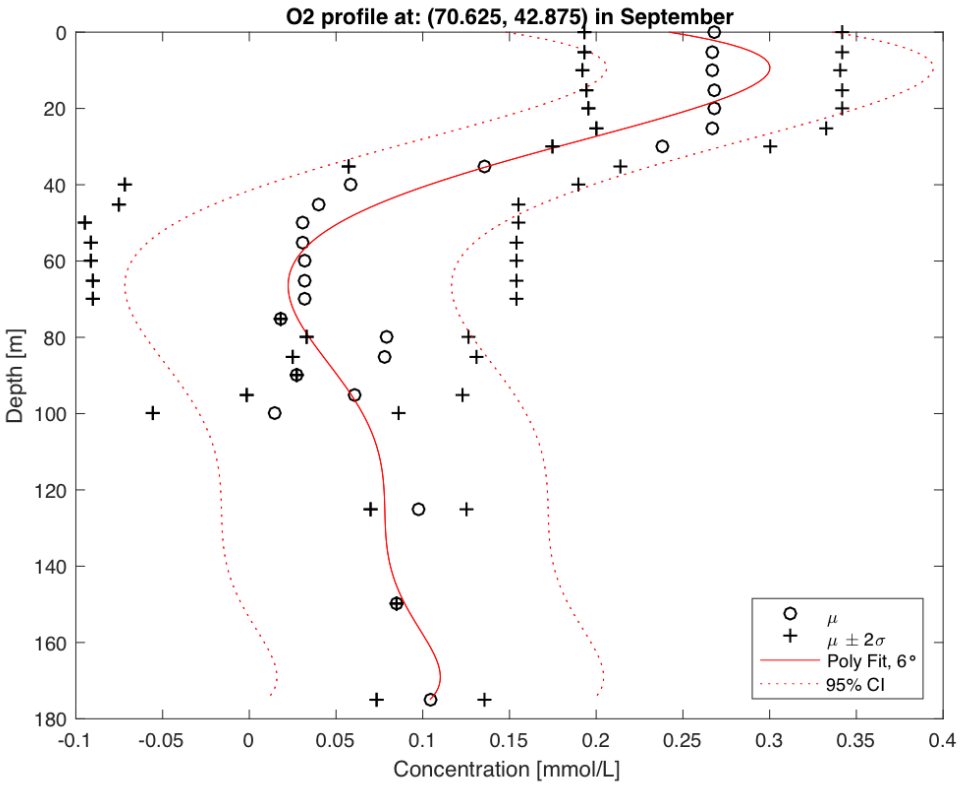

Figure 24: O2 concentration profile derived from World Ocean Atlas data. The mean and 2 standard deviations are circles and crosses respectively. The six-degree polynomial fit and 95% confidence intervals are solid red and dotted red lines respectively.

The artificial seep was deployed off the coast of New Hampshire several times over two days in late October 2017 for this experiment. Data from the first day of deployments was assessed prior to the second day to improve the focus of the next data set collection. Three bubble sizes of each gas, argon and nitrogen, were created at four second intervals in 55 meters of water. The cadence of four seconds was chosen based on conservative estimate of the limit of vertical, range, resolution of the ES18 transducer. With a bandwidth of 8kHz, this transducer has a resolution of approximately 10cm, and the bubbles of these sizes rise at a rate of roughly 20cm/s. Releasing a bubble every four seconds, spaced them far enough apart in the water column to be individually observed by the sonar, without interfering with each other or violating the resolution limit of the

system. Individual deployments were performed for each bubble size rather than scripting the sizes for specific time periods. This strategy was employed to minimize excess data at an individual size, and guarantee that enough data were acquired at each size of each gas in real time. The decision could be made based on real time assessment of acquired data to switch sizes. Figure 25 shows an echogram of the 2.4mm nitrogen bubbles created.

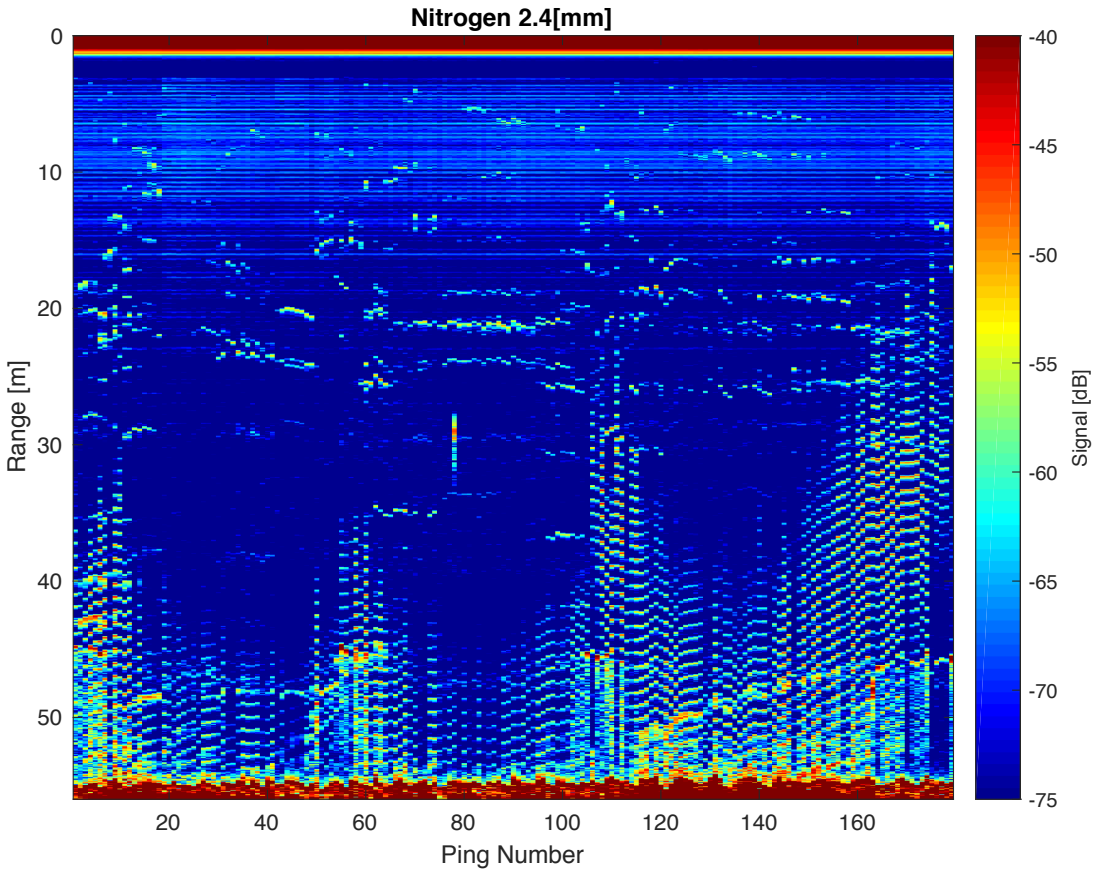

Figure 25: Echogram from ES18 transducer from all pings containing 2.4mm Nitrogen bubbles.

The individual bubbles are spaced at a near constant distance throughout the water column. Fish and other scatterers are also visible in throughout the first water column. The strong contiguous horizontal target at ~45 meters is the floating pickup line attached to the artificial seep. While this

echogram appears continuous, it is an amalgamation from four instances or realizations of the bubbles of this size and gas observed in the water column. Finding the seep within the beam of the transducer is a complicated procedure, resulting in a large record without bubbles in the beam. For conciseness, the data containing bubbles are lumped together. Additional echograms of all the data used in this analysis are presented in Appendix A.

The maximum return from each bubble is picked first by using the findpeaks MATLAB function, which searches for local maxima in each individual ping. The thresholds input into this function used to pick bubbles are the minimum amplitude, -70dB, the minimum distance between the local maxima, 24points, and the maximum width of the peaks width, 20points. The range which the algorithm operates over is manually limited in each ping. After the automatic selections, erroneous results, such as a fish or the pickup line, were manually removed based on a priori knowledge of these phenomena and their appearance in the echogram when visually examining all the pings at once. Picks which persisted across several pings with a constant spacing between picks and the knowledge of fish and other scatterers were the major factors in eliminating selections which were not on bubbles. Figure 26 shows the picked points for the above data with white x's overlaid.

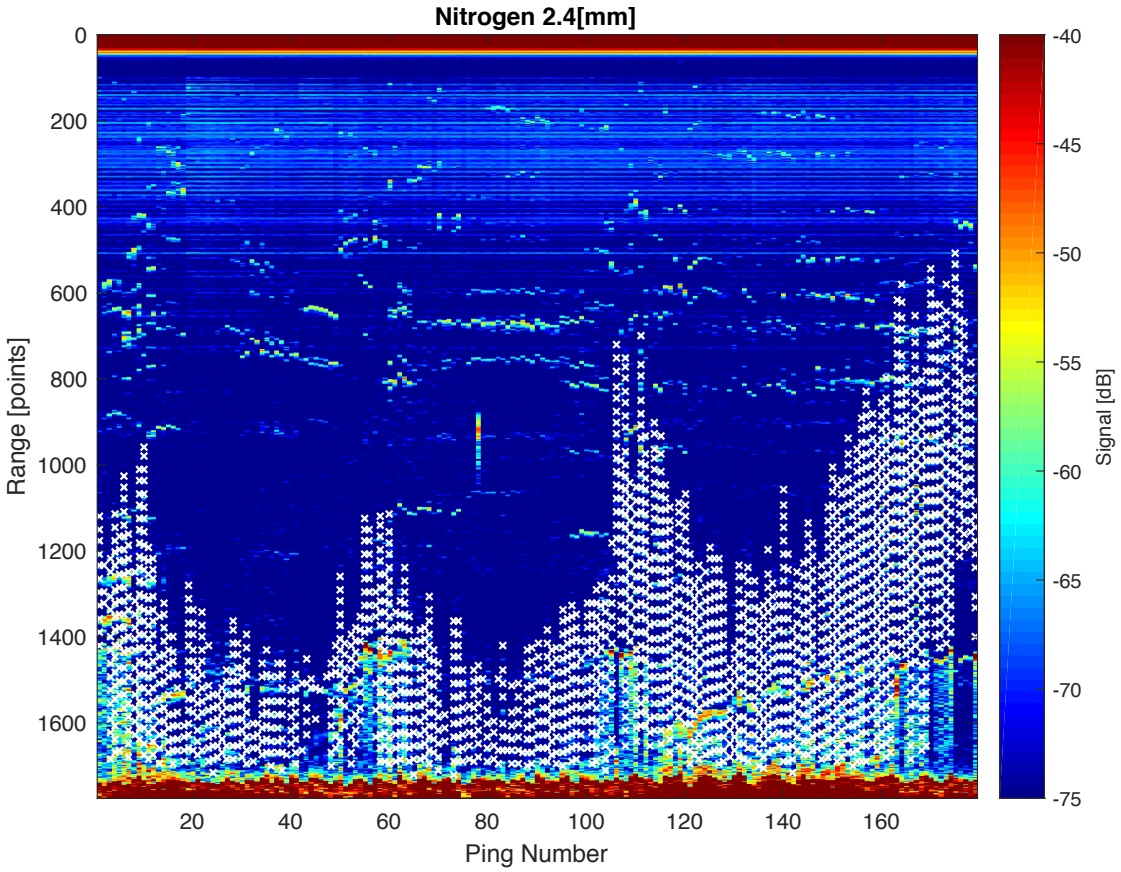

Figure 26: Echogram form ES18 transducer from all pings with 2.4mm Nitrogen bubbles. Overlaid as white x's are the individual points picked for each bubble.

The corresponding along and athwart phase angles are selected from the same location of these maxima. These two angles are input into equation 17, resulting in a correction factor for each of the targets within the beam. This correction factor is subtracted off the signal amplitude to attain the target strength. This is repeated for both argon and nitrogen and each of the three bubble sizes created. The resultant target strength values are binned in five meter increments and plotted vertically in box plots in Figure 27. These data can be compared directly to the output of the

expected values derived from the dissolution and target strength models for bubbles of theses sizes and gas compositions.

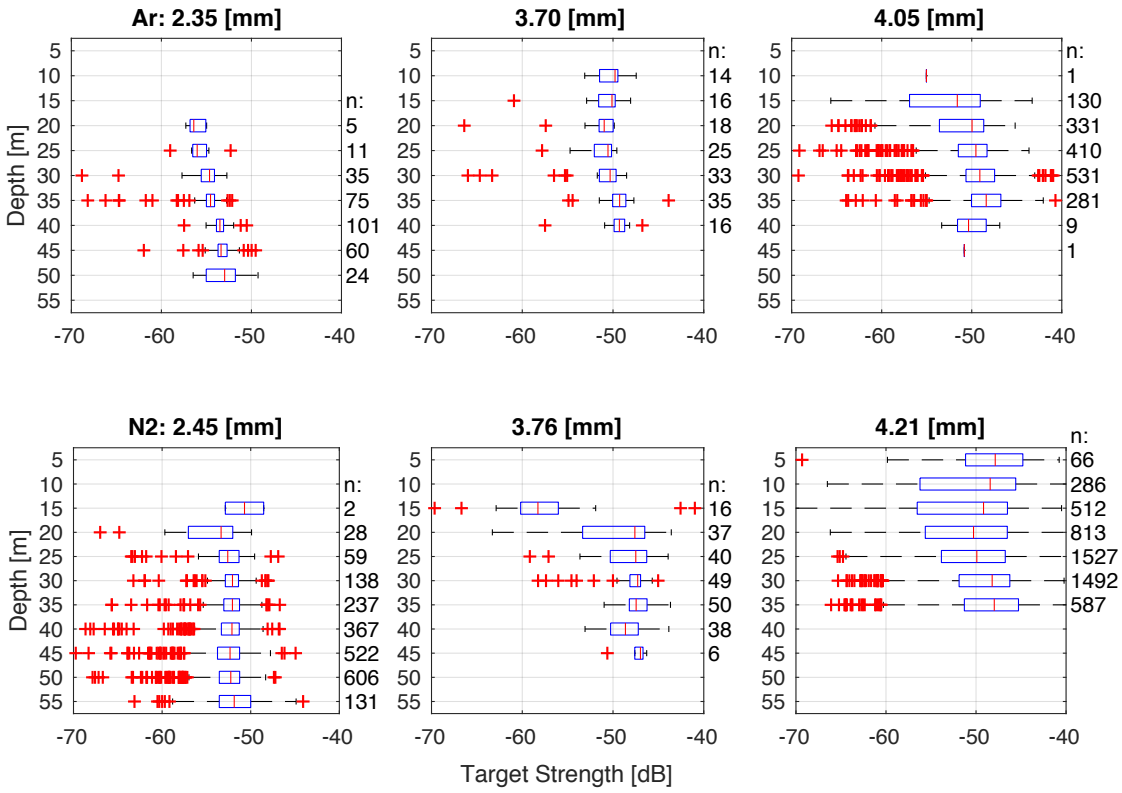

Figure 27: Target strength from all seeps in five meter bins. Argon bubble sizes in the top row, Nitrogen in the bottom row. Red vertical lines are median values per bin, boxes are 25th to 75th percentiles, whiskers contain 99.3% of all the data, red crosses represent the remaining 0.7%. The number of samples in each bin is displayed on the right.

iv. Data and Model Comparison

The target strength estimates for argon and nitrogen bubbles of three sizes shown in Figure 27 are the main data result from this study. The variability in the data could depend where in the beam the bubble was ensonified as all data are included. The main beam of the ES18 lies within 11±2 degrees, or 6.5deg about the maximum response axis (MRA) circularly. Outside of this beam, the

response of the transducer drops off dramatically, and the correction factor becomes more extreme. To determine the angle where the data become less reliable, the data were binned by integer angle and subtracted from the target strength profile, Figure 28 illustrates the angular dependence of the mismatch. The deviations from the model are static below approximately 9 degrees for each dataset. Therefore, this angle was chosen as the cutoff, so bubbles which are greater than 9 degrees from the MRA were not included in subsequent analysis.

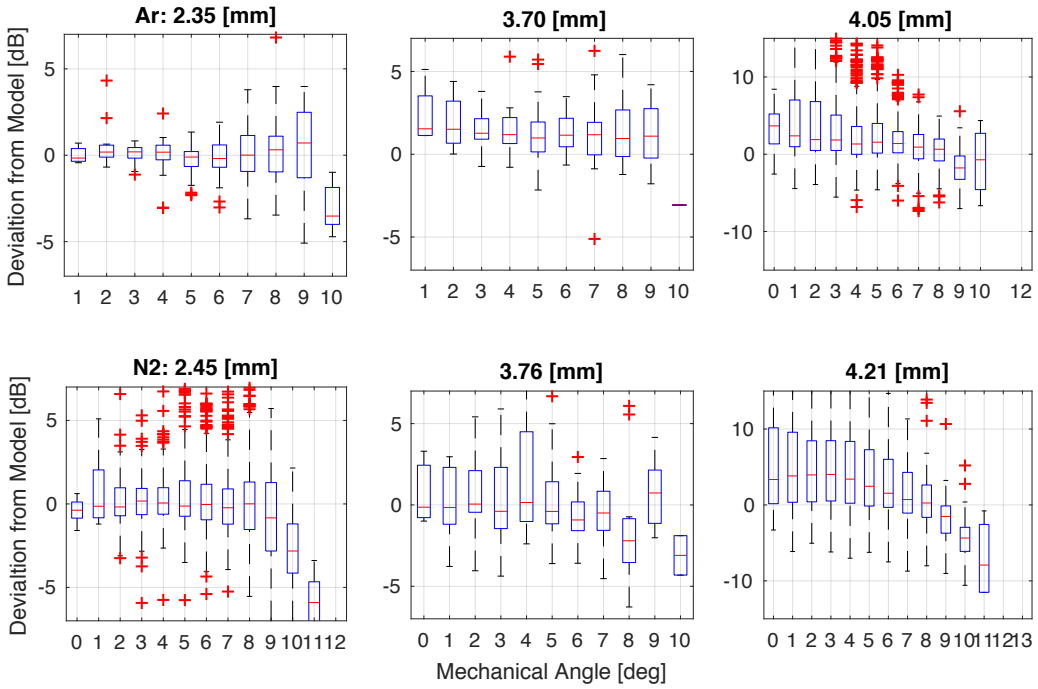

Figure 28: Angular dependence of deviation from model. Box plots binned per integer angle, red vertical lines are median values per bin, boxes are 25th to 75th percentiles, whiskers contain 99.3% of all the data, red crosses represent the remaining 0.7%. Nitrogen data are the bottom row, bubble sizes from smallest to largest, left to right. Argon data are on the top row, sizes from smallest to largest, left to right. Data remain static up to 9 degrees.

The data presented in Figure 27 were designed to test both the dissolution and target strength models simultaneously by using targets of known composition and size. The field calibration values for each bubble size and gas shown in Figure 13 were used to seed the dissolution model in

a similar fashion to the original simulations illustrated in Figure 1. Then the bubble's size and composition is evolved, from this well-defined initialization, as it rises through the water column characterized by the CTD data from Figure 23. The evolution was performed using both the modified McGinnis and TAMOC bubble dissolution models. The resultant estimate of effective radius over depth for these bubbles is converted to target strength based on the size and gas composition, Figure 2, through equations 7 and 8, resulting in an output akin to the simulated prediction in Figure 6. The results from this calculation are overlaid on the main resultant data in Figure 29. For both argon and nitrogen, each bubble size is an individual subplot of target strength vs. depth in 5 meter bins. The output of the McGinnis evolution model are solid black lines, while the TAMOC model are dashed lines. The data from the smallest bubble sizes of each gas align with the models quite well where the largest deviations are less than ~2dB. The medium and largest bubble sizes appear to be biased low. This mismatch is likely due to the bubbles fracturing either at the orifice upon creation, due to a damaged solenoid, or a slightly obstructed orifice, or during the ascent to the surface. Obstruction of the exhaust solenoid from particulate may have caused fracturing by separating the flow. However, fracturing may not account for the full variability in these data. The larger non-spherical larger bubbles could scatter differently enough to cause variation due to their complex geometry. The nitrogen and argon smallest bubble size data are separate enough to be clearly distinguished from one another throughout most of the water column.

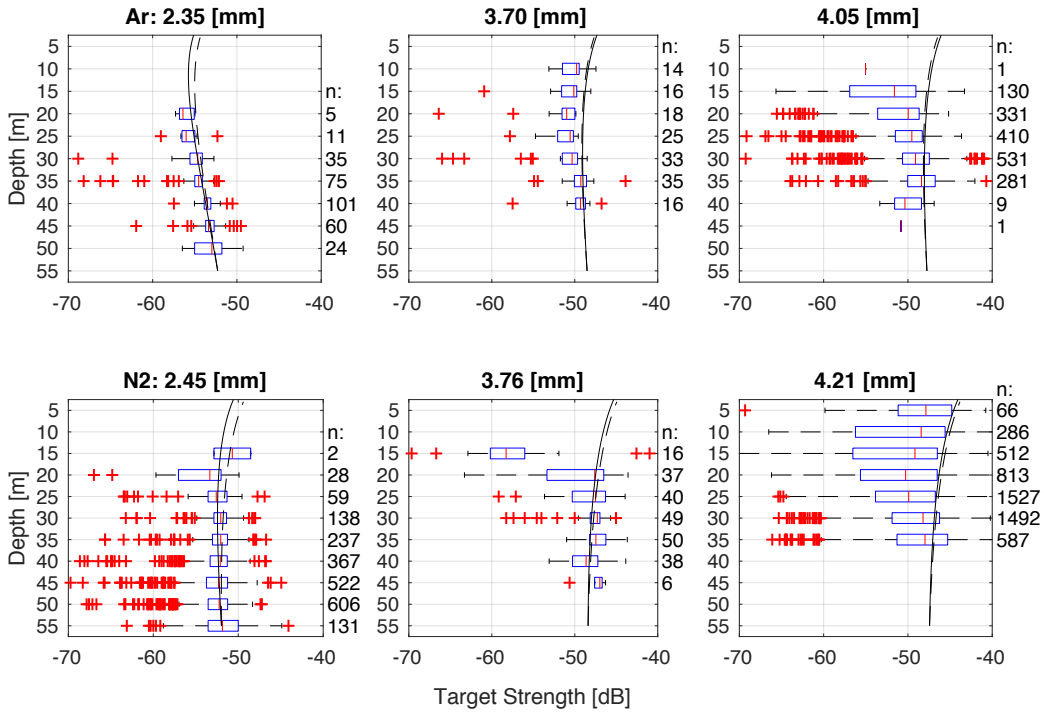

Figure 29: Estimated target strength vs. depth. Box plots binned per angle, red lines are median values, boxes are 25th to 75th percentiles, red crosses are outliers. Nitrogen data are the bottom row, bubble sizes from smallest to largest, left to right. Argon data are on the top row, sizes from smallest to largest, left to right. Modified McGinnis model as solid black line, TAMOC model as dashed black line. The number of bubbles in each bin is listed on the right side of each plot.

Comparing the data-model differences directly by subtracting the acoustic target strength of each individual bubble from the estimated target strength predicted by the model, residuals are produced for each data set. The distributions of these residuals are grouped by bubble size and gas, since the depth dependency is removed. Figure 30 shows the kernel density functions, effectively a smoothed distribution of the residuals, for each gas and bubble size in decibels, and their mean values. Note that most of the peaks of these distributions are centered close to zero, however some of the larger bubbles have wide tail distributions which trend low. The peak centers and low tails of the larger bubble sizes due to model mismatch are again indicative of fracturing bubbles at the orifice or in the water column.

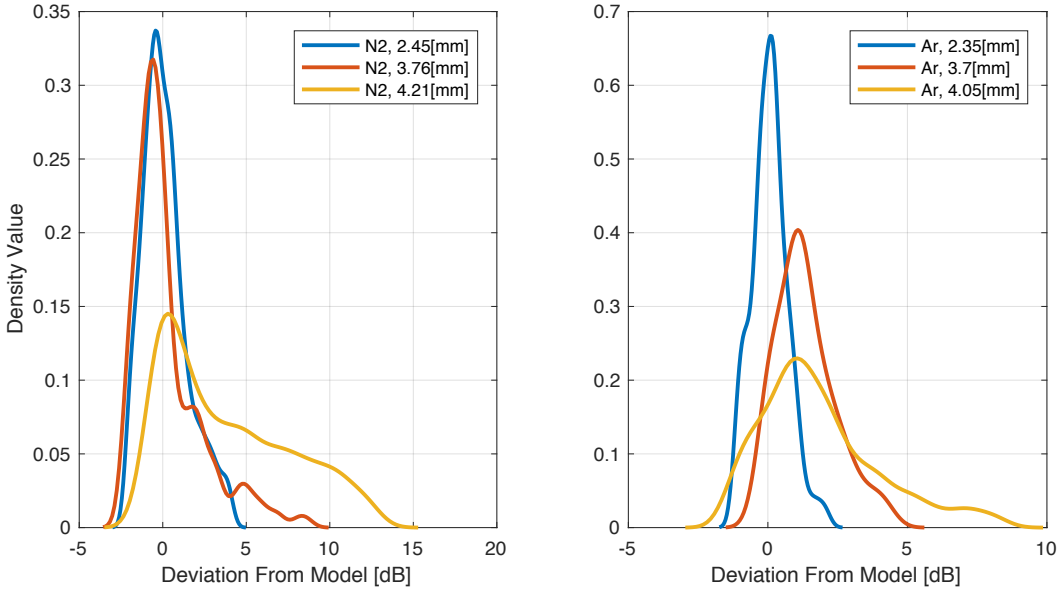

Figure 30: Kernel density function of model deviations for each of the six groups, nitrogen(left), argon(right).

Converting the distributions in target strength to uncertainty values in millimeters is calculated by subtracting the measured backscattered cross section from the estimated values from the model for each individual bubble [Weidner 2018]. This uncertainty in bubble radius is given by equation 18:

$$\sigma_a = \frac{da}{d\sigma_{bs}} \sigma_{\sigma_{bs}} \quad [18]$$

where σ_a is the standard deviation of the bubble radius, $\frac{da}{d\sigma_{bs}}$ is the change in that radius with respect to the change in cross section, and $\sigma_{\sigma_{BS}}$ is the standard deviation of the cross sections for a bubble. Equation 7 gives the backscatter cross section for a bubble in relation to its radius, a, over the denominator involving a ratio of resonant and incident frequencies and damping coefficients, δ^2. Since we are well above resonance for these bubbles, f is much larger than f_r, so that $\left(\frac{f_r}{f}\right)^2 \gg 1$. Using this assumption applied to equation 7, results in equation 19:

$$\sigma_{bs} = \frac{a^2}{1+\delta^2} \quad [19]$$

Applying equation 18, results in the derivative, equation 20:

$$\frac{d\sigma_{bs}}{da} = \frac{2a}{1+\delta^2} \quad [20]$$

If the damping coefficients are assumed to be very small, $\frac{da}{d\sigma_{bs}} = \frac{1}{2a}$, the expected uncertainty in a bubble radius estimate can be obtained, yielding equation 21 [Weidner 2018].

$$\sigma_a = \frac{da}{d\sigma_{bs}}\sigma_{\sigma_{BS}} = \frac{\sigma_{\sigma_{BS}}}{2a} \quad [21]$$

Computing these values for the mean, μ_a, and standard deviation, σ_a, for each gas and bubble size over all depths, 0-55[m], results in table 2:

Table 2 Uncertainty Estimates, Standard Deviation of Individual Observations:

	$\mu_a \pm \sigma_a(2.4[\text{mm}])$	$\mu_a \pm \sigma_a(3.7[\text{mm}])$	$\mu_a \pm \sigma_a(4.2[\text{mm}])$
Argon	-0.0038 ± 0.30[mm]	-0.4289 ± 0.60[mm]	-0.4059 ± 1.18[mm]
Nitrogen	0.05372 ± 0.67[mm]	0.09343 ± 1.42[mm]	-0.7571 ± 1.81[mm]

To gain an idea of the confidence in the mean value, the number of measurements is incorporated to use the metric of standard error, simply dividing the standard deviation from table 2 by the square root of the number of measurements, $SEM = \frac{\sigma_a}{\sqrt{N}}$, resulting in table 3:

Table 3 Uncertainty Estimates, Standard Error of the Mean for Individual Observations:

	$\mu_a \pm \text{SEM}_a(2.4[\text{mm}])$	$\mu_a \pm \text{SEM}_a(3.7[\text{mm}])$	$\mu_a \pm \text{SEM}_a(4.2[\text{mm}])$
Argon	-0.0038 ± 0.01704[mm]	-0.4289 ± 0.04798[mm]	-0.4059 ± 0.02868[mm]
Nitrogen	0.05372 ± 0.01478[mm]	0.09343 ± 0.09263[mm]	-0.7571 ± 0.02496[mm]

The uncertainty values in table 2 represent the standard deviation of the differences between the estimated and the measured backscatter cross-sections, $\sigma_{\sigma_{bs}}$, from all bubbles divided by two times

the effective radius, a. The pattern of increasing uncertainty with increasing bubble size is expected, as the target strength values for larger bubbles are more similar.

V. Discussion

The target strength values for the medium and largest bubble sizes are lower than expected. The video from the camera on top of the synthetic seep suggests that these bubbles may have been fracturing at the orifice. This could also occur while traveling throughout the water column. The larger less spherical bubbles could be scattering in a more complex way which would violate the spherical assumption made by the models and add variability to the data. Based on the uncertainty of these data in table 2, fracturing would seem a more likely explanation. If the bubbles were not fracturing, the uncertainty may be lower. If the signal was still well below the expected target strength values without fracturing, and a lower uncertainty, new implications could be made about the estimates of methane flux from bubbles of these sizes. The continued investigation into the synthetic seep's operation may lead to a more detailed explanation of the fracturing, however initial findings would indicate that the solenoid may have been mechanically damaged from to an over pressurization due to a failed pressure regulator. An alternate theory involves some small amounts of salt water entering the solenoid, during the purge procedure performed multiple times in the lab and at sea, which caused buildup and more turbulent or restricted flow patterns through the exhaust solenoid. The velocity of the flow is much higher at the greater differential pressures required to create large bubbles, which accentuates this mechanical problem. After the field experiment, gas bubble fracturing upon exit were observed of in tank tests, further suggesting that the solenoid had been compromised. The exhaust solenoid was replaced based on these findings.

Figure 31 illustrates molar concentration estimates of each gas constituent from the bubbles created as they rise through water column. Based on the valid measurements between the 2.45mm N_2 and 2.35mm Ar bubbles, these concentrations appear accurate. Argon exchanges much more gas compared to nitrogen, due to the lower concentration of argon in the surrounding water. This is illustrated by a higher influx of nitrogen and outflow of argon from the argon bubbles figure 31(left), compared to the flux from nitrogen bubbles(right). The flux of argon and nitrogen out of the bubble and into the surrounding water through the gas-water interface is shown in figure 32. These bubbles were all predicted to survive to the surface, which implied that the remaining content of each gas is released into the atmosphere.

The water column data from the ES18 transducer aligns with both the McGinnis and TAMOC evolution models, and the Medwin target strength model for the 2.4mm bubbles. The validation of these models for this bubble size implies that the methods for quantifying the flux from methane seeps using this transducer are valid. The separation between the argon dissolution curve, used as a close surrogate for methane, and the nitrogen curve also suggests that the evolution is valid for gases like methane which have relatively low aqueous concentrations.

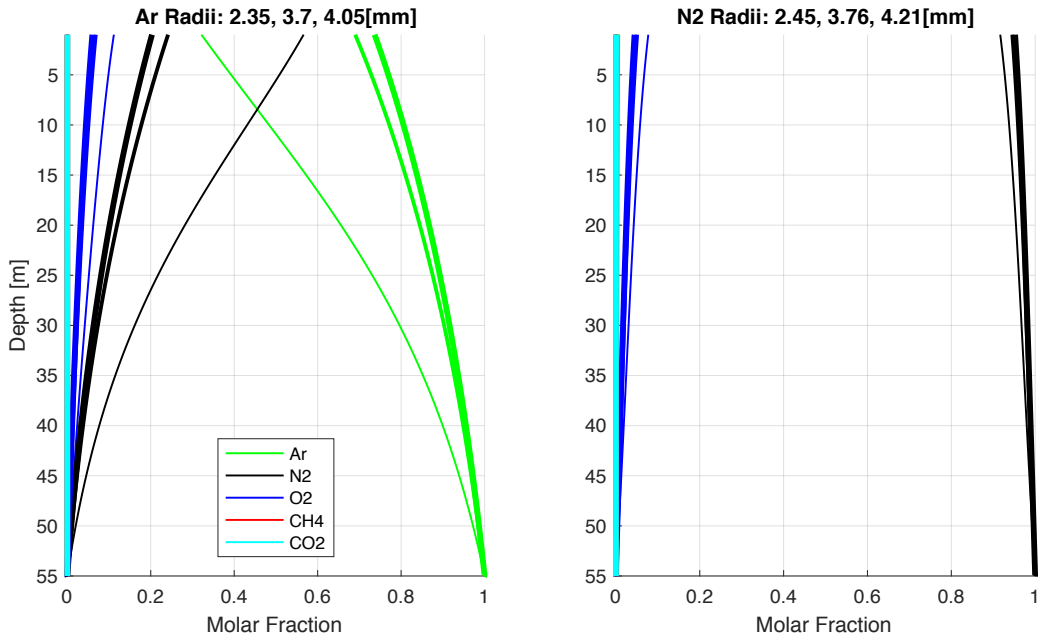

Figure 31: Modeled molar fractions of each constituent gas throughout the water column. Each color denotes a different gas, where linewidth corresponds to effective bubble radius, wider lines are larger radii. The other minority gasses are accounted for here, but effectively are not visible since their contribution is minimal.

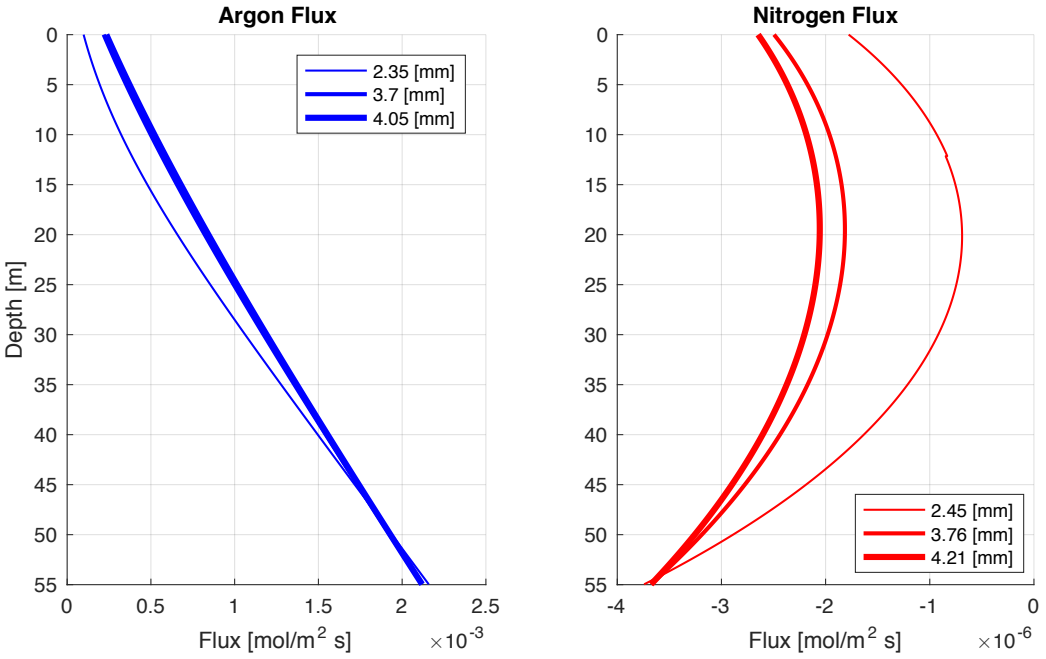

Figure 32: Flux of each gas into the water column over depth. The linewidth corresponds to the effective bubble radius. Note that argon flux is three orders of magnitude larger than Nitrogen.

The ES18 transducer and EK80 wide band transceiver is a common system used in previous studies for methane flux quantification [Jakobsson et al. 2015, Weber et al. 2014, Weidner 2018]. These model validations further solidify estimates of methane gas flux from these studies. Acoustic systems with lower frequencies could be used to attempt to find the resonance peaks of bubbles in this size range as they rise through the water column. With multiple samples of a bubbles traverse, the chances of observing a resonance peak due to the controlled nature of the seep are much higher. This would be useful for verification of the target strength models in the resonance region. While the use of a low frequency projector and four hydrophones as a pseudo split aperture correlator was attempted during this study, ultimately the SNR was not high enough for meaningful results. Additional studies performed at greater depths would also be beneficial as the greater amount of water column surveyed, the more complete picture of a bubble's evolution is captured. With additional time and distance travelled in the water, larger differences in bubble size throughout the water column could be observed.

This experiment was limited to two days of observations in shallow waters off the coast of New Hampshire. The validity of the models was tested in the conditions found in this water mass. The assumptions made for this water may not hold true in regions with warmer or colder water, or where greater oxygen gradients due to local production or consumption. The bubbles tested were created through a clean orifice, but may have picked up some surfactants as they rose through the water column. There is video evidence of particulate in the water column from the GoPro recording on the synthetic seep. Ultimately these data are attempting to validate measurements made on methane bubbles, however argon and nitrogen were used. While argon served as a suitable surrogate, it is not a direct comparison as pure methane since methane is more reactive,

combustible, and has marginally different compressibility and thermal properties. Many of these complications could be addressed in ongoing studies.

VI. Conclusions

A synthetic seep system was designed and constructed for studying the methodologies quantifying the flux of methane from gaseous seeps. The system performance was modeled and characterized. Acoustic data from 2.35mm radii argon bubbles, and 2.45mm radii nitrogen bubbles generated by the synthetic seep agree with existing bubble evolution and target strength models. This validates the spherical approximations made in both the mass transfer and various acoustic scattering properties. Based on the uncertainty of 0.3mm and 0.67mm, these data add confidence to the claims by previous studies which use similar methods for methane flux approximations. The discernable difference between N_2 and Ar, where argon was used as a surrogate for methane dissolution, adds confidence to the gas transfer in the evolution model for clean bubbles released from shallow water depths.

The synthetic seep system was built for studying the methodologies quantifying the flux of methane for gaseous seeps. This project is under continuing development which may lead to further study of these models in other conditions. This system will be deployed and measured with other acoustic systems where some improvements may be made. Near term plans involve deployment off the coast of New Zealand on an oceanographic cruise aboard a larger vessel, which will involve greater water depths.

VII. References

Beater, P. Pneumatic Drives. System Design, Modeling, and Control. New York: Springer, 2007

Collett, T. S., et al., 2009, Natural Gas Hydrates: A Review, in T. Collett, A. Johnson, C. Knapp, and R. Boswell, eds., Natural gas hydrates—Energy resource potential and associated geologic hazards: AAPG Memoir 89, p. 146– 219

Clay, C., and H. Medwin (1977), Acoustical Oceanography: Principles and Applications, pp. 194–201 and 461–469, New York: John Wiley & Sons.

Demer, D. A., L. Berger, M. Bernasconi, E. Bethke, K. Boswell, D. Chu, R. Domokos, A. Dunford, S. Fäaaler, S. Gauthier, L. T. Hufnagle, J. M. Jech, N. Bouffant, A. Lebouges-Dhaussy, X. Lurton, G. J. Macaulay, Y. Perrot, T. Ryan, S. Parker-Stetter, S. Stienessen, T. Weber, and N. Williamson (2015), Calibration of acoustic instruments, ICES Cooperative Research Report No. 326, 133 pp.

Dickens, G. R., J. R. O'Neil, D. K. Rea, and R. M. Owen (1995), Dissociation of oceanic methane hydrate as a cause of the carbon isotope excursion at the end of the Paleocene, Paleoceanography, 10(6), 965–971, doi:10.1029/95PA02087.

Foote, K. G., H. P. Knudsen, and G. Vestnes (1987), Calibration of Acoustic Instruments for Fish Density Estimation: A Practical Guide, International Council for the Exploration of the Sea, Copenhagen.

Gidlund P L (1977) Auslegung pneumatischer Schaltungen – Sizing pneumatic components. Proc Internationale Fachtagung zur Systemschau "Antreiben – Steuern – Bewegen", Hannover, pp 240-261

Gruber, Nicolas. "The marine nitrogen cycle: overview and challenges. "*Nitrogen in the marine environment* (2008): 1-50.

ISO 6358-3:2014. *Pneumatic fluid power – determination of flow-rate characteristics of components using compressible fluids – Part 3: Method for calculating steady-state flow-rate characteristics of systems.* International Organization for Standardization, Geneva.

MathWorks, (2009). *Bioinformatics Toolbox: User's Guide (R2009b)*. Retrieved February 24, 2018 from: <https://www.mathworks.com/help/physmod/simscape/ref/constantareapneumaticorificeiso6358.html#br7047w-1>

Jakobsson, M., Nilsson, J., Anderson, L., Backman, J., Björk, G., Cronin, T.M., Kirchner, N., Koshurnikov, A., Mayer, L., Noormets, R., O'Regan, M., Stranne, C., Ananiev, R., Macho, N.B., Cherniykh, D., Coxall, H., Eriksson, B., Flodén, T., Gemery, L., Gustafsson, Ö., Jerram, K., Johansson, C., Khortov, A., Mohammad, R. and Semiletov, I., 2015, Evidence for an ice shelf covering the central Arctic Ocean during the penultimate glaciation, *Nat. Com.*, 7, 10365, doi:10.1038/ncomms10365

Johnson BD, Cooke RC. 1981 Generation of stabilized microbubbles in seawater. Science **213**, 209–211. doi:10.1126/science.213.4504.209

Judd, A.G. (2004). Natural seabed gas seeps as sources of atmospheric methane, *Environmental Geology, 46*(8), 988-996

Leifer, I., and I. MacDonald (2003), Dynamics of the gas flux from shallow gas hydrate deposits: Interaction between oily hydrate bubbles and the oceanic environment, Earth Planet. Sci. Lett., 210(3-4), 411–424. doi:10.1016/S0012-821X(03)00173-0

Leifer, Ira, and Ranjan Kumar Patro. "The bubble mechanism for methane transport from the shallow sea bed to the surface: A review and sensitivity study." *Continental Shelf Research* 22.16 (2002): 2409-2428.

Leifer, I., G. de Leeuw, and L.H. Cohen, 2003: Optical Measurement of Bubbles: System Design and Application. *J. Atmos. Oceanic Technol.,* **20**, 1317–1332, https://doi.org/10.1175/1520-0426(2003)020<1317:OMOBSD>2.0.CO;2

Leifer, I., and K. Wilson (2004), Quantified oil emissions with a video-monitored, oil seep-tent, *Marine Technology Society Journal*, 38(3): 44-53.

Liss, P.S., 1973. Process of gas exchange across an air–water interface. Deep-Sea Research 20, 221–238.

McGinnis, D.F. , Greinert, J., Artemov, Y., Beaubien, S.E., &Wüest, A.N.D.A.(2006). Fateofrising methane bubbles in stratified waters: How much methane reaches the atmosphere? . *Journal of Geophysical Research: Oceans (1978–2012), 111(C9).*

Orbey, Hasan, and Stanley I. Sandler. *Modeling vapor-liquid equilibria: cubic equations of state and their mixing rules*. Vol. 1. Cambridge University Press, 1998.

Rehder, G., Brewer, P.W., Peltzer, E.T., & Friederich G. (2002).Enhanced lifetime of methane bubble streams within the deep ocean. *Geophysical research letters*, *29*(15), 21-1.

Römer, M., H. Sahling, T. Pape, G. Bohrmann, and V. Spieß (2012b), Quantification of gas bubble emissions from submarine hydrocarbon seeps at the Makran continental margin (offshore Pakistan), J. Geophys. Res. Oceans, 117, doi:10.1029/2011JC007424.

Sanville, F. E. "A New Method of Specifying the Flow Capacity of Pneumatic Fluid Power Valves." Paper D3, p.37-47. BHRA. Second International Fluid Power Symposium, Guildford, England, 1971

Socolofsky, S. A., A. L. Dissanayake, I. Jun, J. Gros, J. S. Arey, and C. M. Reddy (2015), Texas A&M Oilspill Calculator (TAMOC): Modeling Suite for Subsea Spills, 38th AMOP Technical Seminar on Environmental Contamination and Response, Vancouver, B. C., Canada, June 2-4.

Seabird Scientific, SBE Data Processing, (2017) Retrieved from: <http://www.seabird.com/sbe19plusv2-seacat-CTD>\

"U.S. Geological Survey Gas Hydrates Project." *The Primer*. 2014. Web. 05 Oct. 2015.

Wang, B., S. A. Socolofsky, J. A. Breier, and J. S. Seewald (2016), Observations of bubbles in natural seep flares at GC 600 and MC 118 using in situ quantitative imaging. JGR: Oceans, 121, doi:10.1002/2015JC011452.

Weber, T.C., Lyons, A.P., Bradley, D.L., 2005. An estimate of the gas transfer rate from oceanic bubbles derived from multibeam sonar observations of a ship wake. J. Geophys. Res. 110 (C04005) http://dx.doi.org/10.1029/2004JC002666.

Weber, T. C., L. Mayer, K. Jerram, J. Beaudoin, Y. Rzhanov, and D. Lovalvo (2014), Acoustic estimates of methane gas flux from the seabed in a 6000 km^2 region in the Northern Gulf of Mexico, Geochem. Geophys. Geosyst., 15, 1911–1925, doi:10.1002/2014GC005271.

Weber, T. C., and Ward, L. G. (2015). "Observations of backscatter from sand and gravel seafloors between 170 and 250 kHz," J. Acoust. Soc. Am. **138**(4), 2169–2180. doi: 10.1121/1.4930185

Weidner, E. (2018). A Wideband Method for Direct Assrssment of Bubble-Mediated Methane Flux. University of New Hampshire, Durham, NH

"World Ocean Database." *World Ocean Database*. NOAA, 9 Apr. 2015. Web. 1 Sept. 2017.

Weiss, RF. 1970. The solubility of nitrogen, oxygen and argon in water and seawater. Deep-Sea Research. 17:721-735.

Yamamoto, A., Y. Yamanaka, and E. Tajika. "Modeling of methane bubbles released from large sea-floor area: Condition required for methane emission to the atmosphere." *Earth and Planetary Science Letters* 284.3 (2009): 590-598.

APPENDIX A: All Other Echograms

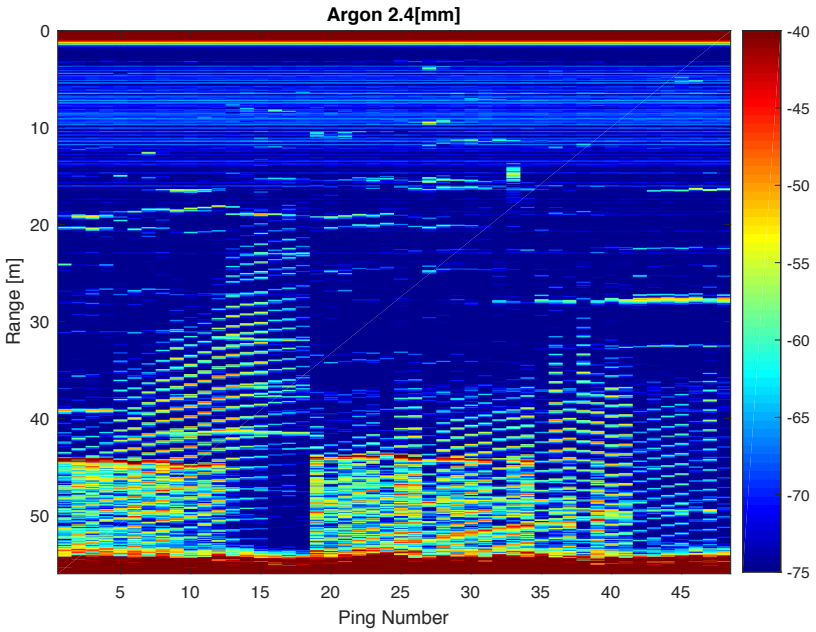

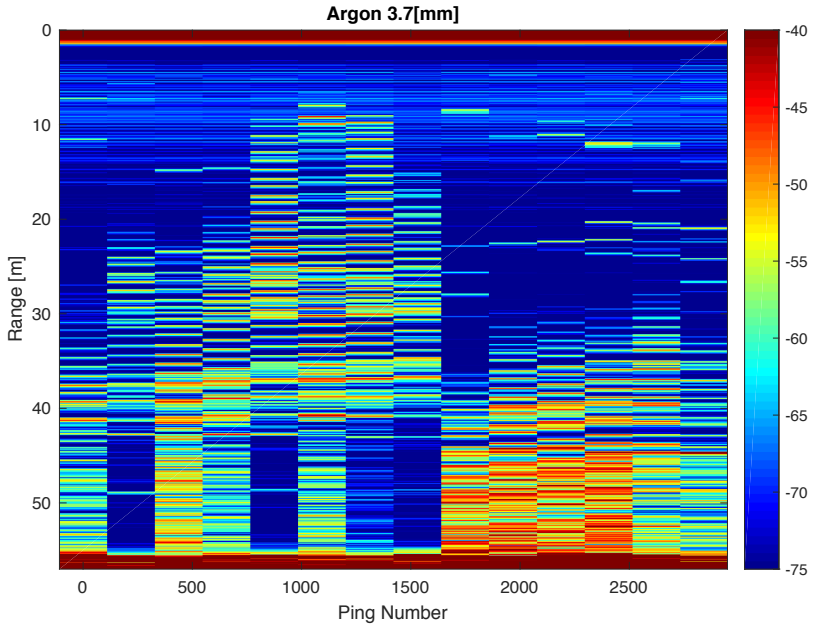

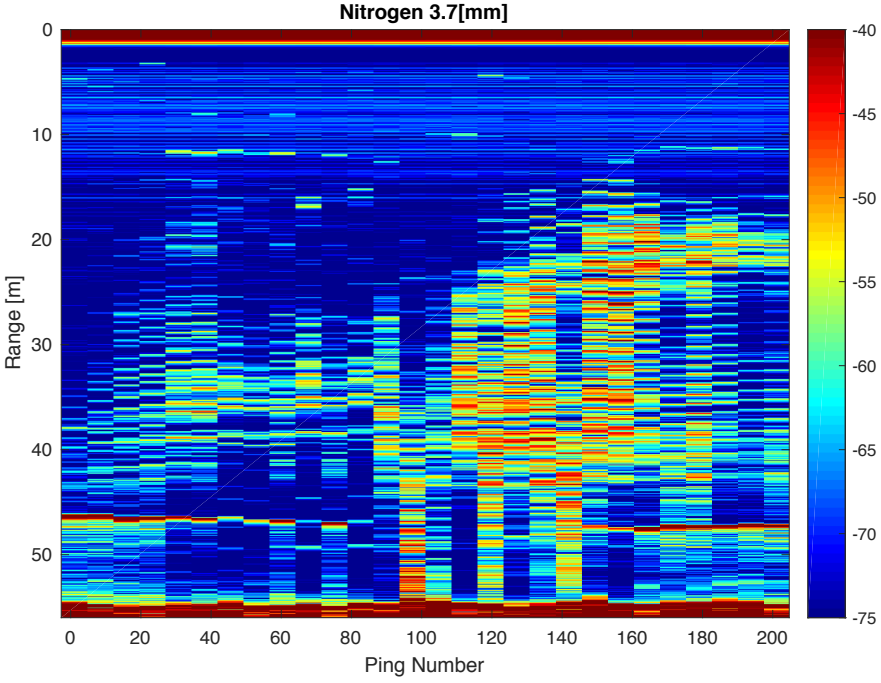
Nitrogen 3.7[mm]
Range [m]
Ping Number
0
10
20
30
40
50
0
20
40
60
80
100
120
140
160
180
200
-40
-45
-50
-55
-60
-65
-70
-75

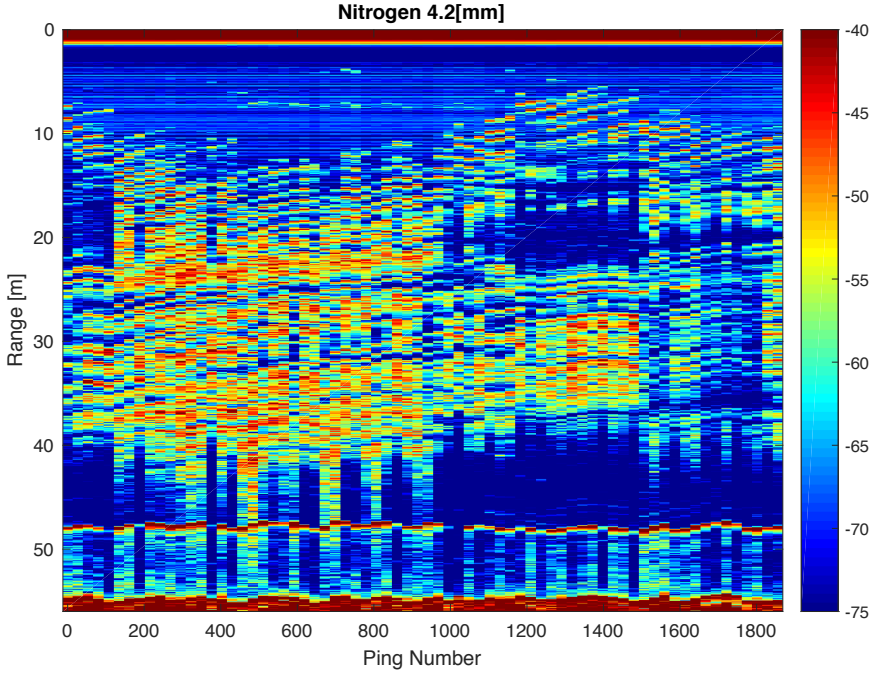
Nitrogen 4.2[mm]
Range [m]
Ping Number
0
10
20
30
40
50
0
200
400
600
800
1000
1200
1400
1600
1800
-40
-45
-50
-55
-60
-65
-70
-75

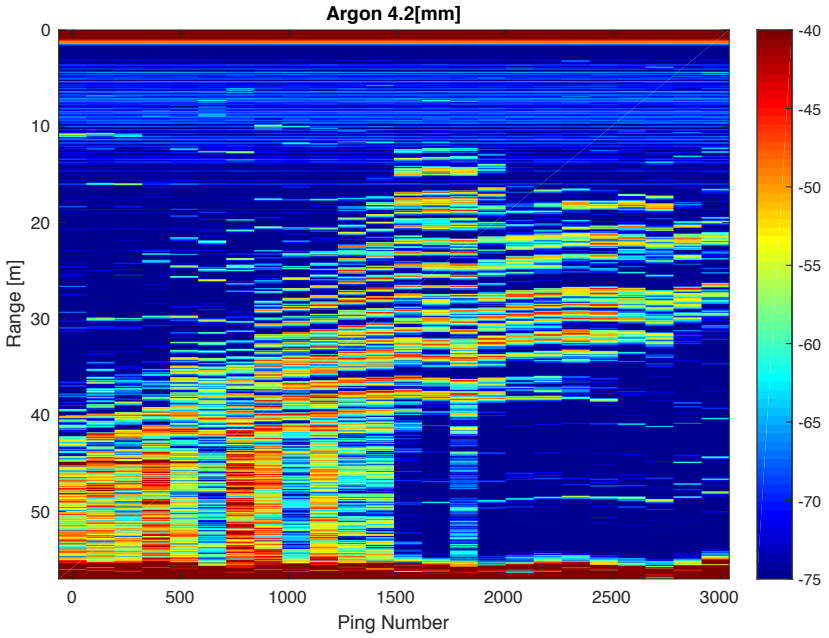
Argon 4.2[mm]
Range [m]
Ping Number
0
10
20
30
40
50
0
500
1000
1500
2000
2500
3000
-40
-45
-50
-55
-60
-65
-70
-75

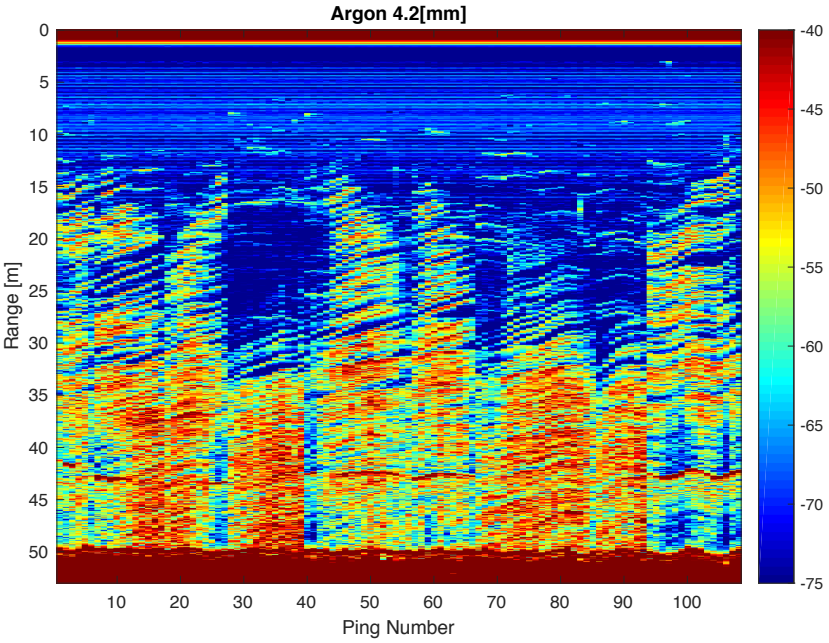
Argon 4.2[mm]
Range [m]
Ping Number
0
5
10
15
20
25
30
35
40
45
50
10
20
30
40
50
60
70
80
90
100
-40
-45
-50
-55
-60
-65
-70
-75

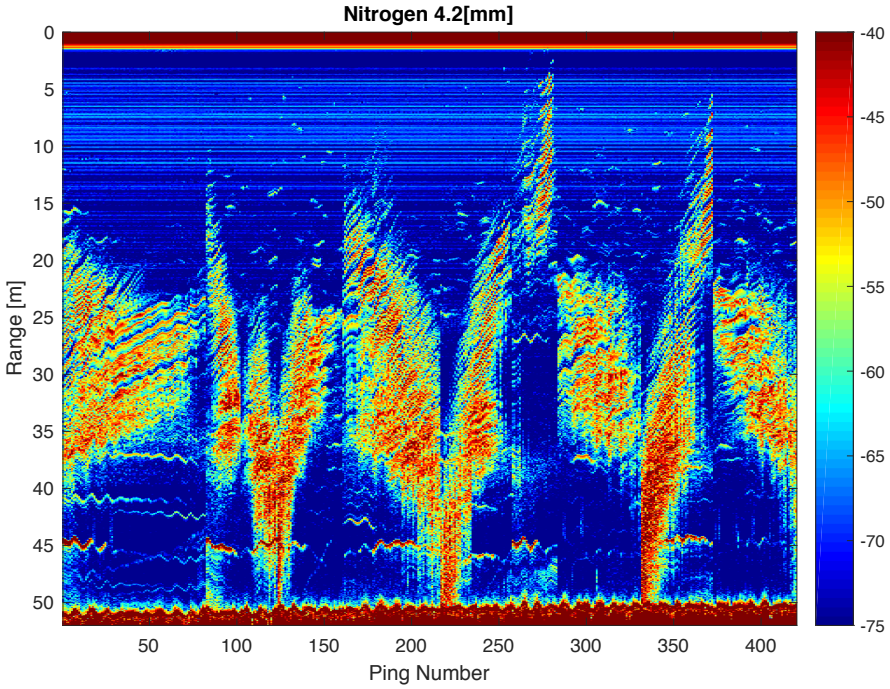
Nitrogen 4.2[mm]
Range [m]
Ping Number
0
5
10
15
20
25
30
35
40
45
50
50
100
150
200
250
300
350
400
-40
-45
-50
-55
-60
-65
-70
-75

APPENDIX B: Bubble Maker Arduino Code

Ardino Codes, Each beginning with “title.c”:

```
//leak_test.c
    void setup() {
  // put your setup code here, to run once:
pinMode(12, OUTPUT);
pinMode(3, INPUT);
Serial.begin(9600);
}
void loop() {
  // put your main code here, to run repeatedly:
  digitalWrite(12, HIGH);
  delay(1000);
int leakValue = digitalRead(3);
if (leakValue == LOW) {
  Serial.println("No Leak");
}
if (leakValue == HIGH) {
  Serial.println("Leak!");
}
}

///*
// Bubble Maker Code, solenoids_deploy.c
// Independently control two solenoid valves by external power sources
// Read voltage from differential pressure gauge and open feed solenoid until requested
differential is reached.
// Written by Kevin Rychert, 2016
// */
// these constants won't change:
// feed solenoid connected to digital pin 10
// injection solenoid connected to digitial pin 9
const int omegaSensor = A0; // the omega is connected to analog pin A0
const float threshold = 20;  // threshold value to decide when the differential pressure is high
void setup() {
  pinMode(11, OUTPUT); // declare the solPin as as OUTPUT
  pinMode(9, OUTPUT); // declare the solPin as as OUTPUT
  //!!! CHECK TO TURN THIS OFF WHEN DEPLOYING -> USE THIS CODE "DEPLOY"
  //Serial.begin(9600); // use the serial port
 // delay(600000); // delay before bubbles making begins 300000ms=5min
}
void loop() {
```

```
//delay(50);// delay to buffer
// read the sensor and store it in the variable sensorValue:
float  sensorValue = analogRead(omegaSensor);
float   psi = sensorValue*50/1024; // convert to psi
delay(50);// delay to buffer
// if the sensor reading is greater than the threshold:
if (psi <= threshold) {
   // Serial.println(psi);
    // update the feed solenoid pin increasing pressure of system:
    digitalWrite(11, HIGH);// open feed solenoid
    delay(4);// how long the feed solenoid is open for
    digitalWrite(11, LOW);//close feed solenoid
    delay(4);// slight delay between opening/closing feed solenoid
    // send the string "Open!" back to the computer, followed by sensor values
    //Serial.println("Open: sensorValue:");
   // Serial.println(sensorValue); // display the value measured by the Omega
    //Serial.println(psi);
}  else {
  digitalWrite(11, LOW);
 // Serial.println("Closed!");
 // Serial.println(psi); // display the value measured by the Omega
  }
delay(50);// delay to buffer
sensorValue = analogRead(omegaSensor); // read sensor again
psi = sensorValue*50/1024; // convert
 // Serial.println(psi); //show updated value
//delay(50);// delay to buffer

// if the differentual pressure is above the threshold
// open solenoid, make a bubble
if (psi >= (threshold-0.05)) {
  digitalWrite(9, HIGH); // open exhaust solendoid, (make one bubble)
  delay(4); // how long exhaust solenoid is open for
  digitalWrite(9, LOW); // close exhaust solenoid
  delay(1000);// # of milliseconds between bubbles, 1000=1[s]
}
}

/*
  solenoid_simple.c
  solenoid conrol only
  modified 2016-02-10
  by Kevin Rychert
 */
```

```
const int omegaSensor = A0; // the omega is connected to analog pin 0
float psi = 0.001;
int sensorValue = 0;
// the setup function runs once when you press reset or power the board
void setup() {
  // initialize digital pin 13 as an output.
  pinMode(11, OUTPUT);
  pinMode(9, OUTPUT);
  Serial.begin(9600);       // use the serial port
}
// the loop function runs over and over again forever
void loop() {
  digitalWrite(11, LOW);
//  digitalWrite(9, LOW);
  delay(5);
  digitalWrite(11, HIGH);
//  digitalWrite(9, LOW);
  delay(4);
  digitalWrite(11, LOW);
//  digitalWrite(9, LOW);
  delay(5);
//
delay(500);
float   sensorValue = analogRead(omegaSensor);
float   psi = sensorValue*50/1024;
Serial.println(sensorValue);
//Serial.println(psi);
delay(1000);
//  delay(100);
}

///*
// Bubble Maker Code, solenoids_test.c
// Independently control two solenoid valves by external power sources
// Read voltage from differential pressure gauge and open feed solenoid until requested
differential is reached.
// Written by Kevin Rychert, 2016
// */
// these constants won't change:
// feed solenoid connected to digital pin 10
// injection solenoid connected to digitial pin 9
const int omegaSensor = A0; // the omega is connected to analog pin A0
//int threshold = 1;  // threshold value to decide when the differential pressure is high
void setup() {
```

```
  pinMode(11, OUTPUT); // declare the solPin as as OUTPUT
  pinMode(9, OUTPUT); // declare the solPin as as OUTPUT
  //!!! CHECK TO TURN THIS OFF WHEN DEPLOYING -> OTHER CODE "DEPLOY"
  Serial.begin(9600); // use the serial port
  //delay(300000); // delay before bubbles making begins
}

void loop() {
delay(50);// delay to buffer
//float ttime = millis();
//float threshold = 1;
//float t1=6000;
//float t2=12000;
//float t3=18000;
//if (ttime<=t1); {//30 minutes in ms
//  threshold = 1;
//}
//if (ttime>t1 & ttime<=t2){;//30 to 50 mins in ms
//  threshold = 15;
//}
//if (ttime >= t3);{ //over 70 mins
//  threshold = 30;
//}
//Serial.println(ttime);
//Serial.println(t1);
//Serial.println(ttime>t1);
float threshold = 5;
// read the sensor and store it in the variable sensorValue:
float  sensorValue = analogRead(omegaSensor);
float   psi = sensorValue*50/1024; // convert to psi
delay(50);// delay to buffer
// if the sensor reading is greater than the threshold:
if (psi <= threshold) {
    Serial.println(psi);
    // update the feed solenoid pin increasing pressure of system:
    digitalWrite(11, HIGH);// open feed solenoid
    delay(4);// how long the feed solenoid is open for
    digitalWrite(11, LOW);//close feed solenoid
    delay(4);// slight delay between opening/closing feed solenoid
    // send the string "Open!" back to the computer, followed by sensor values
    Serial.println("Open: sensorValue:");
   // Serial.println(sensorValue); // display the value measured by the Omega
    Serial.println(psi);
}  else {
```

```
  digitalWrite(11, LOW);
  Serial.println("Closed!");
  Serial.println(psi); // display the value measured by the Omega
  }
delay(10);// delay to buffer
sensorValue = analogRead(omegaSensor); // read sensor again
psi = sensorValue*50/1024; // convert
Serial.println(psi); //show updated value
delay(5);// delay to buffer

// if the differentual pressure is above the threshold
// open solenoid, make a bubble
if (psi >= (threshold-0.05)) {
  digitalWrite(9, HIGH); // open exhaust solendoid, (make one bubble)
  delay(4); // how long exhaust solenoid is open for
  digitalWrite(9, LOW); // close exhaust solenoid
  delay(1000);// # of milliseconds between bubbles, 1000=1[s]
}
}
```